RSC Advances

ROYAL SOCIETY OF CHEMISTRY

www.rsc.org/advances

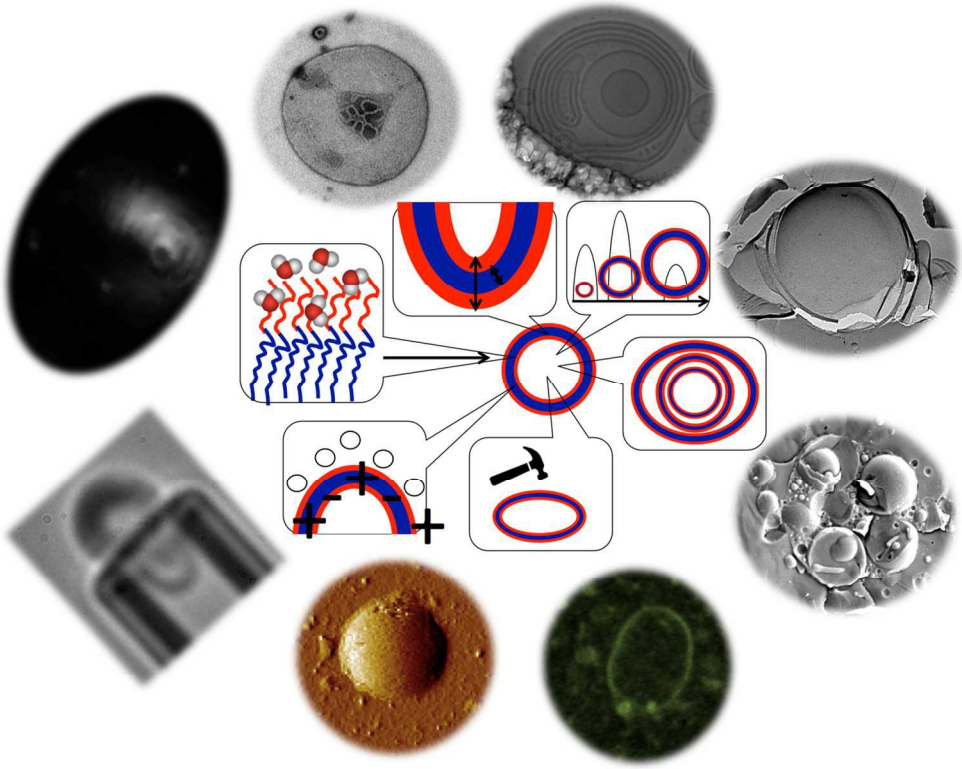

We present 17 techniques to analyze polymersomes, in terms of their size, bilayer properties, elastic properties or surface charge.

516x401mm (72 x 72 DPI)

Journal Name

ARTICLE TYPE

Cite this: DOI: 10.1039/xxxxxxxxxx

Selecting analytical tools for characterization of polymersomes in aqueous solution†

Joachim Habel,[ab] Anayo Ogbonna,[b] Nanna Larsen,[c] Solène Cherré,[d] Søren Kynde,[e] Søren Roi Midtgaard,[e] Koji Kinoshita,[f] Simon Krabbe,[g], Grethe Vestergaard Jensen,[e] Jesper Søndergaard Hansen,[h] Kristoffer Almdal,[d] and Claus Hélix-Nielsen*[abi]

Received Date
Accepted Date

DOI: 10.1039/xxxxxxxxxx

www.rsc.org/journalname

Selecting the appropriate analytical methods for characterizing the assembly and morphology of polymer-based vesicles, or polymersomes are required to reach their full potential in biotechnology. This work presents and compares 17 different techniques for their ability to adequately report size, lamellarity, elastic properties, bilayer surface charge, thickness and polarity of polybutadiene-polyethylene oxide (PB-PEO) based polymersomes. The techniques used in this study are broadly divided into scattering techniques, visualization methods, physical and electromagnetical manipulation, sorting/purification, and simulation tools. Of the analytical methods tested, Cryo-TEM and AFM turned out to be advantageous for polymersomes with smaller diameter than 200 nm, whereas confocal microscopy is ideal for diameters $>$ 400nm. Polymersomes in the intermediate diameter range can be characterized using FF-Cryo-SEM and NTA. SAXS provides reliable data on bilayer thickness and internal structure, Cryo-TEM on multilamellarity. Taken together, these tools are valuable for characterizing polymersomes per se but the comparative overview is also intended to serve as a starting point for selecting methods for characterizing polymersomes with encapsulated compounds or polymersomes with incorporated biomolecules (e.g. membrane proteins).

1 Introduction

Polymersomes are hollow spheres arising from spontaneous self-assembly of amphiphilic block copolymers in solution[1–15]. They have the potential to replace liposomes in biomolecule encapsulation for drug delivery applications[16–20], for incorporating proteins in their bilayer for creating artificial cells[14,21–24] and as design elements in ion-[25,26] and water selective biomimetic membranes[27–31].

In order to use these versatile nanoscopic tools, a reliable and reproducible characterization is crucial. The characterization of polymersomes is however often a compromise between the convenience of instrumentation and preparation on one side and precision of the measurements on the other. More precise techniques typically implicate more invasive sample preparation. Here we summarize analysis techniques in five thematic groups with overlapping borders as shown in Figure 1 and summarized in Table 1: Scattering techniques, visualization methods, physical and electromagnetical manipulation, sorting/purification, and simulation tools.

Among all methods, dynamic light scattering (DLS) is the most convenient technique for routine supplementary size and morphology measurements (resolution limit: 2 nm). DLS is based on the scattering of laser light at different intensity induced by the brownian motion of particles in solution. Velocity and therewith particle size is calculated from these intensity flucuations, using the Stokes-Einstein relation[32]. DLS is simple and fast, how-

[a]Technical University of Denmark, Department of Environmental Engineering, Miljøvej, building 113, 2800 Kgs. Lyngby, Denmark. Tel: +45 27 10 20 76; E-mail: clhe@env.dtu.dk
[b]Aquaporin A/S, Ole Maaløes Vej 3, 2200 Copenhagen, Denmark.
[c]University of Copenhagen, Copenhagen Biocenter, Ole Maaløes Vej 5, 2200 Copenhagen, Denmark.
[d]Technical University of Denmark, Department of Micro- and Nanotechnology, Produktionstorvet, building 423, 2800 Kgs. Lyngby.
[e]University of Copenhagen, Niels Bohr Institute, Hans Christian Ørsted building D, Universitetsparken 5, 2100 Copenhagen, Denmark.
[f]University of Southern Denmark, Department of Physics, Chemistry and Pharmacy, Campusvej 55, 5230 Odense, Denmark.
[g]University of Copenhagen, Department of Biology, August Keogh Building, Universitetsparken 13, 2100 Copenhagen, Denmark.
[h]Lund University, Department of Experimental Medical Science, Box 117, 22100 Lund, Sweden.
[i]University of Maribor, Laboratory for Water Biophysics and Membrane Processes, Faculty of Chemistry and Chemical Engineering, Smetanova ulica 17, 2000 Maribor, Slovenia

† Electronic Supplementary Information (ESI) available: Polymersome images of NTA, NS-TEM, Cryo-TEM, FF-TEM, Cryo-FF-SEM, CLSM, AFM, modelling of small-angle scattering, videos of NTA, CLSM and micropipette aspiration analysis. See DOI: 10.1039/b000000x/

Table 1 Tabularic overview of the most relevant characterization methods for polymersomes respectively liposomes. Abbreviations are listed in the Abbreviations section. The size detection limit (SDL) responds to resolution limit for the visualization methods, atomic force microscopy (AFM) and scanning tunnelling microscopy (STM), respectively the diameter of the smallest detectable particle for all other methods. In the case of visualization methods, Small-angle x-ray and neutron scattering (SAXS and SANS) that were used in the study, the SDL is measured from own experiments.

Characterization method	Subgroup	SDL [nm]	Parameters for analysis	Advantages	Disadvantages	References
Scattering methods						
Dynamic light scattering		2	Size	Simple	Only for monodisperse samples	39–41
Quasi-Elastic light scattering				Minimal sample volume	Difficult comparison between instruments	
Photon correlated spectroscopy				Sensitivity to few large vesicles	Misinterpretation of aggregates	
Static light scattering	Multi-angle light scattering	10	Molecular weight, radius of gyration	Simple	RI and concentration required	42,43
X-ray scattering	Small-angle X-ray scattering	0.5	Bilayer thickness, lamellarity, encapsulation	Single polymer residue information	Elaborated setup	33,44–47
X-ray scattering	Wide-angle X-ray scattering	0.05	Structural information	Atomic resolution	Elaborated setup	43,48
Neutron scattering	Small-angle neutron scattering	0.5	Bilayer thickness, lamellarity, encapsulation	Single polymer residue information	Elaborated setup & sample preparation	47,49–51
Stopped-flow light scattering			Permeability	Simple	Only for monodisperse samples	52
Nanoparticle tracking analysis		70	Size, concentration	Simple	Underestimation of small vesicles	37,53,54
				High accuracy	Misinterpretation of vesicles in z-plane	
Visualization methods via photons				Native environment	Resolution limit	
Optical microscopy		200	Size, concentration	Widely available	Low contrast	55
Optical microscopy	Phase-contrast microscopy	200	Size, concentration	Better contrast	Additional staining	55–57
Fluorescence microscopy	Generalized polarization microscopy		Size, lamellarity, concentration	Specific labeling	Photobleaching	43,58
				Multiple staining	Only for labelled vesicles	
				Exquisite sensitivity	Phototoxic effects	
Fluorescence microscopy	Fluorescence correlation spectroscopy		Size, lamellarity, concentration	Can distinguish free & incorporated dye		59
Fluorescence microscopy	Confocal laser scanning microscopy	200	Size, lamellarity, concentration	High sensitivity	Difficult quantitative analysis	54,60,61
				Improved signal-to-noise-ratio		
Fluorescence microscopy	Stimulated emission depletion microscopy	20	Size, lamellarity, concentration	Resolution	Elaborated setup	62
Visualization methods via electrons				Resolution	In vacuum	
				Contrast	Elaborative sample preparation	
Transmission electron microscopy	Negative-staining TEM	0.5	Size, morphology, lamellarity	Resolution	Staining artifacts	37,49,52
					Vesicle shrinkage	
Transmission electron microscopy	Freeze fracture TEM	0.1	Size, morphology, lamellarity	Structure preservation	Freezing artifacts	49,63,64
					Uncertainty in true size	
Transmission electron microscopy	Cryo-TEM	0.1	Size, lamellarity, morphology	Structure preservation	Freezing artifacts	49,65
					Uncertainty in bilayer thickness	
Scanning electron miscroscopy	Freeze fracture Cryo-SEM	2	Size, lamellarity, morphology	3D appearance	Freezing artifacts	66,67
Scanning electron microscopy	Environmental SEM	30	Size, lamellarity, morphology, concentration	Native environment	Poor resolution	40,60,68
Electromagnetic manipulation methods						
Scanning probe microscopy				3D information	High sensitivity to vibration	
Scanning probe microscopy	Atomic force microscopy	1	Size, topology, elastic properties	Sensitivity	Shape alteration upon attachment	37,40,54,60,69
	Scanning force microscopy				Amphiphile adsorption on cantilever	
Scanning probe microscopy	Scannig tunneling microscopy	0.1	Size, topology	No mechanical contact to sample	Cantilever tip condition crucial	70,71
Nuclear magnetic resonance	P^{31}-nuclear magnetic resonance		Lamellarity	High accuracy	Signal decrease due to convenient buffer	72–74
Electron paramagnetic resonance			Encapsulation, bilayer flexibility,			40,75,76
Electron spin resonance			bilayer polarity, lamellarity	Specific to unpaired electrons	Signal decrease due to water	
Laser doppler electrophoresis			Zeta potential, surface charge potential	Fast	Calibration required frequently	77,78
Optical tweezer			Elastic properties	High sensitivity	Elaborated aligment	79
Mechanical manipulation methods						
Tether pulling			Elastic properties	Vesicle directly accessible	Only for large vesicles	79
Micropipette aspiration		2500	Elastic properties	Vesicle directly accessible	Only for large vesicles	79,80
Falling-ball viscosimetry			Elastic properties	Vesicle directly accessible	Only for large vesicles	79
Sorting methods						
Flow cytometry	Fluorescence-activated cell sorting	270	Size, concentration	Obtaining multiple properties	RI required	39,53,81,82
				Widely available	Size restriction	
Field flow fractionation	Asymmetric flow field-flow fractionation	1	Size, concentration	Wide range of vesicle sizes	Elaborated setup	39,49
					Calibration standard necessary	
					Sample loss through adsorption	
Size exclusion chromatography		17	Size, concentration	Well-established	Not for large vesicles	39,83–85
					Amphiphile adsorption on column material	
					Calibration standard necessary	
					Slow amphiphile diffusion	
Size exclusion chromatography	High performance liquid chromatography	1	Size, concentration	More selective & rapid than SEC	Elaborated setup	84
Tunable resistive pulse sensing		70	Size, concentration	Accurate for concentration measurement	Potential pore clogging	53,54
Coulter counting					Only for monodisperse samples	
Tunable resistive pulse sensing	Scanning ion occlusion sensing	50	Size, concentration	High sensitivity	Calibration required	54,86
Simulation methods						
Molecular dynamics			Structural information	Highest resolution	Elaborated calculation	87
Molecular dynamics	Coarse grain molecular dynamics		Structural information	Simpler than MD	Less accurate than MD	88
Molecular dynamics	Dissipative particle dynamics		Structural information	Simpler than coarse grain	Less accurate than coarse grain	89

ever care has to be taken when interpreting polydisperse samples, which are the case with most polymers and most preparation methods. Small-angle X-ray[33] or neutron scattering (SAXS or SANS; resolution limit of both: 0.5 nm)[34] provide detailed information about the polymersome bilayer[35], but due to the need for access to large scale radiation facilities, their use for routine measurements for their information is somewhat limited. With SAXS and SANS, particle shape and size information are collected by monitoring the elastic X-ray respectively neutron scattering at low angles (0.1-10°). X-ray interact with the electron clouds of molecules or elements, where neutrons interact with the nuclei[33,34]. Another scattering method for polymersome permeability measurements is stopped-flow light scattering (SFLS). The mechanism behind SFLS is a rapid mixing of the polymersome solution with an osmotically active substance, called osmotic agent (usually sucrose or NaCl). The osmotic shock causes the polymersomes to change volume, resulting in changed light scattering, which is monitored by a photomultiplier tube collecting 90° angle scatter from the mixing chamber. Thus, osmotically induced polymersome shrinking leads to increased light scattering. Nanoparticle tracking analysis (NTA), a novel analysis method[36–38], combines scattering and visualization. This method assesses the hydrodynamic diameter of single particles in a bulk solution without influence of density or refractive index in contrast to DLS. Particle-induced scattered laser light is captured by a CCD camera, where each particle is tracked separately. Their size is again calculated by the Stokes-Einstein relation[36]. To our knowledge this is the first publication, where polymersomes have been analyzed using the NTA technique.

Generally, electron microscopy (EM), especially transmission electron microscopy (TEM, resolution limit: 0.1-0.5 nm) is the most frequently used in-depth analysis technique for size, morphology, lamellarity or bilayer thickness. Almost all studies on polymersomes and other self-assembly morphologies are based on TEM. Image formation in TEM is based on sample interaction of electrons transmitting through a thin sample slice. Regions of high electron density in the sample (strong interaction) appear as black, whereas regions of low electron density (low interaction) are white[90]. The same holds for scanning electron microscopy (SEM), but here the electrons are not passing the sample but interact and excite sample atoms that emits so-called secondary electrons that give information about the sample electron density dependent on their energy[91]. To improve contrast, sample are stained with electron-rich heavy metal atoms, gathering around particles and emphasize their shape in the image (negative staining, NS). The great drawback is that EM (with exception of environmental scanning electron microscope, ESEM[92]) only works under vacuum conditions. To overcome vacuum-induced sample deformation, the sample is quick-frozen in liquid alkanes in order to capture them in original shape in liquid solution and observed at -180°C (Cryo-SEM or -TEM). Optionally the sample can be fractured to reveal the particle interior (freeze fracture, FF-SEM or -TEM)[93]. Optical microscopy can visualize polymersomes in their native environment however the main size dimension of interest (nm range) is below the diffraction limit of photons. There are two fluorescence-mediated optical microscope techniques used in this study: Confocal laser scanning microscopy (CLSM) and generalized polarization microscopy (GPM). CLSM can maximize image resolution within the diffraction limit by optical sectioning, where only focal plane "sample slices" are taken sequentially and in this case visualized by fluorophore laser excitement[94]. GPM is based on the emission of the polarity sensitive fluorophore 6-lauroyl-2-(dimethylamino)-naphthalene (Laurdan) that exhibits a red shift with increasing environment polarity[95]. To overcome the diffraction limit, super-resolution microscopes, mainly based on fluorescence signaling, has been developed[62]. However, the required use of fluorophores comes with additional mixing and purification steps, limiting the use for routine measurements.

Besides EM, atomic force microscopy (AFM, resolution limit: 1 nm) has become a versatile tool for routine measurements, especially on size and topographic information. AFM utilizes an elastic lifting arm (cantilever) with a microscopic tip scanning the sample at small distance using a piezoelectric device. Generally, when the tip interacts with the sample, the cantilever bends and this is monitored by a change of the laser reflection on the cantilever surface, resulting in topographical information about the sample[96]. There are various operation modes. The greatest advantage and disadvantage at the same time is the sensitivity of the cantilever tip. It enables atomic resolution imaging, but is prone to vibration noise and undesired sample interactions[80,97]. All mechanical-based manipulation techniques (tether pulling[98], micropipette aspiration[99] and falling-ball viscosimetry[100]) can be used complementary to AFM but are usually limited to micrometer-sized polymersomes[79]. Micropipette aspiration, used in this study, provides information about the elastic properties of particles by micropipette suction. Here, the particle surface is aspirated into a micrometer-sized glass tube while the leading edge of its surface is monitored[99]. Other bilayer properties such as lamellarity, polarity and zeta potential can be obtained as well by utilization of the electron or nuclear spin after applying an electrical field (electron paramagnetic resonance (EPR)[72,76,101], nuclear magnetic resonance (NMR)[72,76,102] or laser doppler electrophoresis (LDE). The latter method, employed in this study, is based on particle movement due to particle charge interaction with an applied electric field. The doppler shift of particle scattered laser light is used to calculate particle velocity (equally to DLS) and zeta potential using the Smulochowski model[78].

Sorting analysis tools such as flow cytometry (FCM), size exclusion chromatography (SEC) and asymmetric flow field-flow fractionation (A4F) are usually combined with light scattering. FCM[103] is used mainly for cell analysis (as well as the most fluorescence microscopes). The main drawback of FCM is the limited detection level which makes detection challenging for polymersome diameter (d_P) less than 300nm. SEC[104] is the most well-established sorting technique, but suffers from polymer adsorption on the column material. A4F[105] has the advantage of separating a wide range of particle size but requires an expensive setup.

Here we attempt to provide a comparative and representative overview of a total of 17 analyzing techniques for polymersomes of a conventional chemistry for polymersome formation (Polybu-

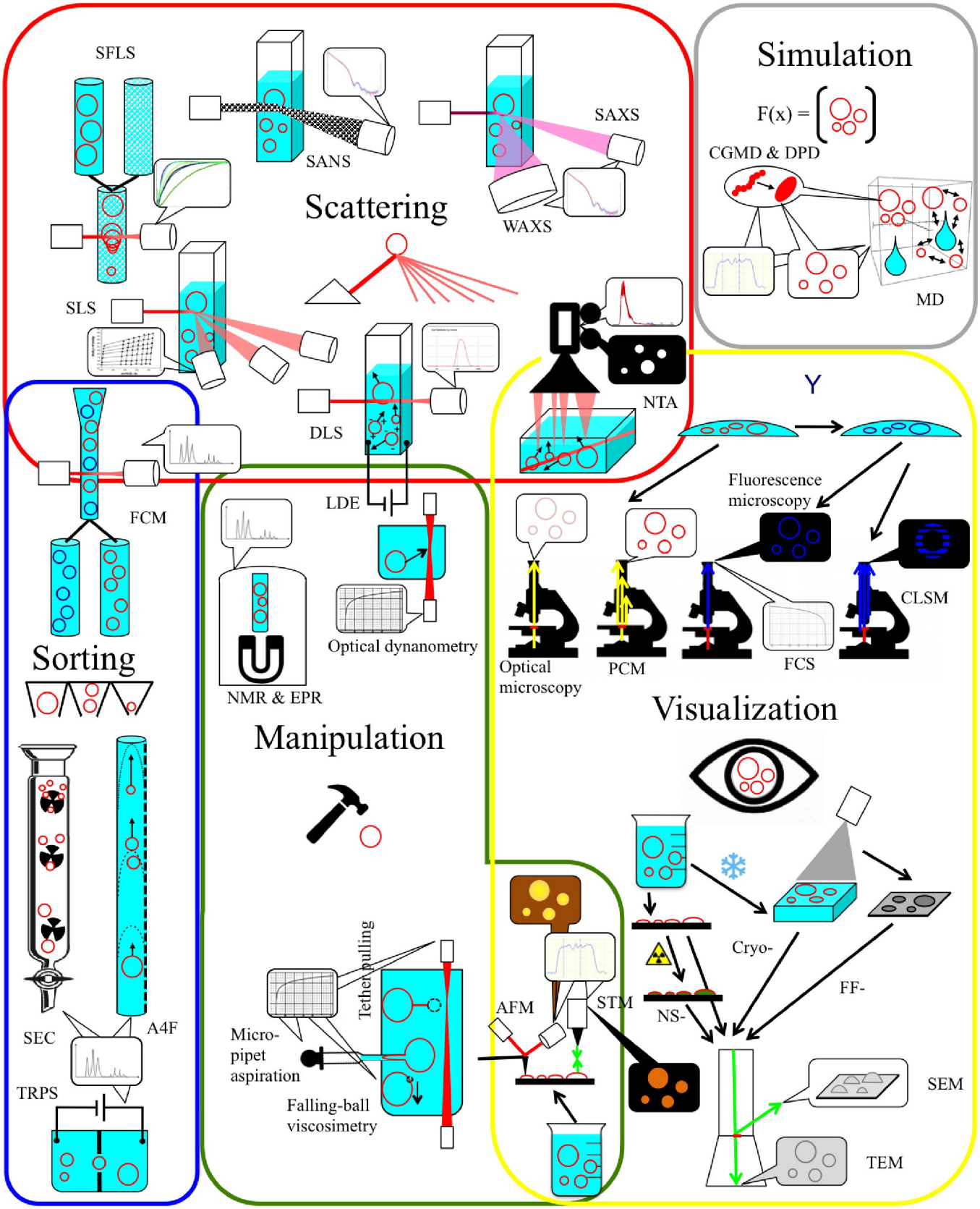

Fig. 1 Schematic overview of the most relevant polymersome analysis techniques. These include scattering-related, visualizing, manipulating, sorting and simulation methods, where there are subgroups on the visualizing elementary particle (electron or photon) or ways of manipulation. The most convenient size analysis technique is Dynamic light scattering (DLS) and most polymersome morphology analyses have been based on transmission electron microscopy (TEM) techniques. All abbreviations are given in the Abbreviations/Nomenclature section

tadiene polyethylene oxide, PB-PEO, chemical structure in Fig. 2) [6,106–108] prepared with a conventional formation method (film rehydration) [8,109,110].

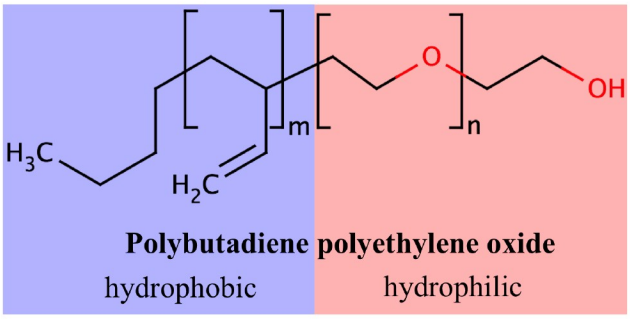

Fig. 2 Chemical structure of polybutadiene-polyethylene oxide (PB-PEO). PB, the hydrophobic has a blue background, PEO, the hydrophilic polymer has red background.

So far there has not been an experimental comparative study on polymersome analysis methods to the extent presented here. Another comparative study with six methods of all families was done by Till et al. [49], however more with a focus on comparing A4F to the other methods than on comparison among them. For liposomes several analytical tools have been investigated [53,60], where CLSM stands out as a particularly popular method. There have also been extensive studies related to specific types of analysis such as EM [64,111], fluorescence microscopy [112], mechanical manipulation [79,80], single particle techniques like NTA [37], AFM [40,113] and scanning tunneling microscopy (STM) [70]. Comparative analysis reviews have been presented for liposomes [39,54], whereas for some polymersome reviews, characterization methods generally only constitute a smaller part of the review, see [8,55].

This work is a step towards integrating all these studies in a more broad perspective. Precision and reliability of a single method can be differentiated better when compared to other methods. A comparison of 17 methods should provide a facilitated insight and also help in deciding when it may be desirable to switch from a fast technique to an in-depth technique. Results here are based upon polymersomes, however in terms of d_P analysis, it also pertains to liposome analysis.

We first analyze methods for determining d_P of PB-PEO polymersomes where DLS, NTA, TEM, NS-TEM, Cryo-TEM, FF-TEM, SEM, FF-Cryo-SEM, CLSM and AFM will be compared. This discussion will be followed by a polymersome lamellarity respectively multivesicularity and bilayer or hydrophobic core thickness (t_P) analysis using Cryo-TEM, AFM, SAXS and SANS. Multilamellar polymersomes are concentric polymersome, where multivesicular polymersomes are randomly encapsulated polymersomes that do not share a common centre. Finally, elastic properties and permeability of the bilayer will be compared using micropipette aspiration and SFLS, wherafter surface charge potential analyzed by LDE and polarity by GPM with Laurdan-labeling will be briefly introduced. Polarity measurements can help to obtain information about the hydrophobic barrier properties, which are essential in drug delivery applications [16]. All measurements were performed on polymersomes formed from PB_{33}-PEO_{18} except polarity experiments (PB_{12}-PEO_9, PB_{22}-PEO_{23}, PB_{46}-PEO_{23}, PB_{46}-PEO_{30}). All measurements on d_P, lamellarity, t_P, zeta potential and polarity were repeated with three independent samples and for all direct measurements (All EM, CLSM and AFM) 100 polymersomes per sample were measured. Micropipette aspiration and AFM were performed with two independent samples.

2 Material & Methods

Polymer synthesis PB_{33}-PEO_{18} was synthesized using anionic polymerization [106]. Butadiene (Bd) and ethylene oxide (EO) monomers were purified and afterwards dried using liquid nitrogen and destilled over *n*-dibutylmagnesium (*n*-Bu_2Mg) and *n*-butyl lithium (*n*-BuLi) to remove any traces of water. Tetrahydrofuran (THF) as the synthesis solvent was purified and dried afterwards via reflux and stirring over sodium in paraffin and benzophenone.

Bd was polymerized first. THF was first introduced in a pre-dried reactor and cooled to -40°C. Afterwards, Bd and *n*-BuLi were added and the reaction was allowed to run for 4 h at -20°C. The polybutadienyl lithium appeared in a orange or yellow colour. The mixture was afterwards cooled again to -40°C and approximately 1ml of EO was added to end-cap the polymerization, visible by the disappearance of the yellow colour. Afterwards, the reaction was left for 1.5h at -40°C, where a precursor was drawn and analyzed via SEC on a SIL-10AD from Shimadzu, Kyoto, Japan. The SEC system consisted of a Shimadzu LC-10AD High performance liquid chromatography (HPLC) pump together with a Viscotek Differential Refractometer model 200 and the following columns: 5 cm Polymer Laboratories, Guard column 3 μm, 30x7.8 cm Waters Styragel HMW 6E, and 30x7.5 cm Polymer Laboratories, PLgel 5 μm Mixed-D. The columns were thermostated at room temperature (RT) during measurement. Non-stabilized THF was used as eluent, and the system was calibrated with polystyrene standard samples having very narrow molar mass distributions. For EO polymerization, the remaining EO was added and 1-*tert*-Butyl-4,4,4-tris(dimethylamino)-2,2-bis[tris(dimethylamino)-phosphor-anylidenamino]-2λ^5,4λ^5-catenadi(phosphazene) (tBuP4) was injected afterwards in a molar *n*-BuLi:tBuP4 ratio of 1:1 to ensure exact stoichiometry [106]. The reaction was heated afterwards to 40°C to start EO chain propagation. Finally, the reaction was quenched with acetic acid after two days. The polymer was precipitated in cold acetone and vacuum dried. Bd-EO stoichiometry was subsequently analyzed by NMR at 300 or 400MHz, wherafter polydispersity index PDI_M was analyzed via SEC. The polymer was stored at -20°C until use. PB_{12}-PEO_9, PB_{22}-PEO_{23}, PB_{46}-PEO_{23}, PB_{46}-PEO_{30} (only used for the polarity measurement using GPM) were purchased from Polymersource, Montreal, Canada. All polymers are listed in table 2.

Polymersome formation via film rehydration PB-PEO and 1,2-dioleoyl-*sn*-glycero-3-phosphocholine (DOPC, Avanti Lipids, Alabaster, USA) was dissolved in $CHCl_3$ to create a 10mg/ml polymer suspension. Afterwards, it was sonicated for 5 min and stored at -20°C until use. 2.5 ml of the stock solution was

Table 2 Polymers used for this study. Polybutadiene$_{33}$-Polyethylene oxide$_{18}$ (PB_{33}-PEO_{18}) was used in all studies except for polarity measurements, where only the other four were used. All values were determined using ^{1}H NMR analysis. M_n stands for number-averaged molecular weight, PDI_M for polydispersity index of the polymer length, defined as M_w/M_n, where M_w stands for weight-averaged molecular weight and f for hydrophilic volume ratio.

Polymer	M_n [g/mol]	PDI_M	f
PB_{12}-PEO_9	1050	1.09	0.319
PB_{33}-PEO_{18}	2561	1.087	0.251
PB_{22}-PEO_{23}	2200	1.09	0.388
PB_{46}-PEO_{23}	3500	1.09	0.233
PB_{46}-PEO_{30}	3800	1.04	0.284

injected in a 5 ml round flask and put afterwards on a rotary evaporator for at least 2 h at room temperature and 2 mbar at a rotation speed of 120 rpm to evaporate $CHCl_3$. The polymer was then present as a smooth film on the flask wall. Afterwards, the sample was rehydrated with 200 μl of tris buffer (10 mM tris pH 8.0, 50 mM NaCl) with 13 mg/ml n-Octyl-β-D-Glucopyranoside (OG) and left stirring at least overnight at RT. The sample was diluted with 800 μl tris buffer (polymersome concentration 25 mg/ml), whereafter 20 mg SM2 biobeads from Bio-Rad, Hercules, USA were added to remove the OG between the polymersome bilayer[52]. Afterwards, the sample was left on a shaker with 200 rpm for 3 h at RT, whereafter another 20 mg of biobeads were added. The sample was then left overnight shaking with 200 rpm at 4°C. Biobeads were removed using a squeezed syringe. Polymersomes prepared by this procedure were used for all analysis techniques except GPM analysis, they were used though for CLSM.

DLS A Nano Zetasizer (Malvern, Worcestershire, UK) was used for DLS experiments. PB_{33}-PEO_{18} polymersomes in tris buffer was injected (1 mL, 0.025 mg/mL) in a disposable cuvette and subsequently measured three times with 6 runs of 10 s per measurement at RT.

NTA For NTA analysis, 0.025 mg/ml PB_{33}-PEO_{18} polymersomes in tris buffer were introduced manually in the analysis chamber of the NTA analysis instrument LM10 (Nanosight, Wiltshire, UK) equipped with a laser of wavelength 638 nm and the NTA software version 3.0. For each samples, three videos of 60 s were recorded with a camera level of 11 and a frame rate of 30 frames/s. The videos were analyzed with a detection threshold of 4 (blur size and minimum track length: auto).

SAXS Prior to SAXS measurement, 20 mg/ml PB_{33}-PEO_{18} polymersomes in tris buffer were dialyzed 1.5 days with a 300 kDa 1ml Float-a-lyzer (VWR, Herlev, Denmark) and subsequently extruded 20 times through track-etched polycarbonate membranes with 200nm pore size. SAXS measurements were performed at the BioSAXS beamline BM29 at the European Synchrotron Radiation Facility (ESRF) in Grenoble, France, and again using the U-SAXS beamline ID02 also at ESRF two days later. Scattering intensity was measured as a function of the magnitude q of the scattering vector given as $q = 4\pi\sin(\theta)/$ where 2θ is the scattering angle and λ is the wavelength of the incoming radiation. The setting at BM29 covered a q-range from 0.04 to 5 nm^{-1} and the ultra small-angle setup at ID02 covered the range from 0.002 to 0.25 nm^{-1} giving a combined q-range from 0.002 to 5 reciprocal nm with a substantial overlap. Data were background subtracted and radially averaged using the standard software at the beamlines. Absolute calibration was done using water as a known scattering standard.

SANS Prior to SANS measurement, 20mg/ml PB_{33}-PEO_{18} polymersomes in deuterated tris buffer were dialyzed 1.5 days with a 300 kDa 1 ml Float-a-lyzer (VWR, Herlev, Denmark), and subsequently extruded 20 times through track-etched polycarbonate membranes with 200 nm pore size. SANS measurements were performed at the Forschungs-Neutronenquelle Heinz Maier-Leibnitz (FRM II), in Munich, Germany. Measurements were performed at three different settings to obtain a large q-range. Sample-detector distances were 1.27, 4 and 8 meter with corresponding collimation lengths of 4, 4, and 8 meter. These settings covered the q-ranges [0.35:4.5] nm^{-1} , [0.12:1.6] nm^{-1} and [0.057:0.77] nm^{-1}. Data were background subtracted and radially averaged using the standard software at the beamline. Absolute calibration was performed using a plexiglass standard.

SFLS A SFM-300 (BioLogic, Claix, France) with a Xe-Hg lamp was used to measure shrinking and swelling of polymersomes. The measured data was fitted to an exponential rise equation to calculate the water permeability of the bilayer P_f, using the following expression[114]:

$$P_f = \frac{k}{(S/V_0)V_W\Delta_{osm}} \quad (1)$$

where k is the rate constant of initial rise in the light scattering curve, S/V_0 the initial surface area to volume ratio of the vesicles, V_w the molar volume of water (18 cm^3/mol) and Δ_{osm} difference in osmolarity[114]. 1M NaCl with tris buffer was used as osmotic agent. 3 ml of 3 mg/ml PB_{33}-PEO_{18} polymersomes in tris buffer was measured at an excitation wavelength of 365 nm, a flow rate of 12 ml/s in 8000 measuring points. 9 traces were averaged with BioKine software. Analysis and normalization of curves was performed with Excel, where the fitting was performed again with BioKine software and Origin.

TEM Eight micro liters MilliQ water were placed on a glow-discharge 400 mesh holey carbon copper grid (Agar scientific, Essex, UK) and blotted off, followed by 3.5 μl of 2.5 mg/ml PB_{33}-PEO_{18} polymersomes in tris buffer that was allowed to adsorb for 2 min. The grid was loaded with another 8 μl MilliQ water to wash out the remaining salt. The grid was placed in CM100 TEM (Philips, Amsterdam, Netherlands) the same day. This TEM has an installed Veleta 2k CCD camera (Olympus, Shinjuku, Japan). The applied voltage on a tungsten source was 80 kV with a 100 μm objective lense aperture.

NS-TEM Eight microliters MilliQ water were dropped on a glow-discharge 400 mesh holey carbon copper grid (Agar scientific, Essex, UK), blotted off and rehydrated twice with 8 μl phosphor tungsten acid. This procedure was followed by injecting 3.5 μl 2.5 mg/ml PB_{33}-PEO_{18} polymersomes in tris buffer with adsorption time of 2 min, followed by washing with 8 μl MilliQ water. Finally, 8 μl phosphor tungsten acid were adsorped for 0.5 min and blotted off afterwards. The grid was placed directly afterwards in the same TEM with the same parameters as for the TEM analysis. Size analysis of the TEM pictures was performed by manual measurement using the image analysis software Gimp 2.8.

Cryo-TEM Three micrometers of 25 mg/ml PB_{33}-PEO_{18} polymersomes in tris buffer was admitted to a glow-discharged 300 mesh holey carbon formvar copper grid (Agar scientific, Essex, UK), mounted on a Vitrobot mark 5 (FEI, Hillsboro, USA). After removal of excessive sample by automated blotting, the sample was rapidly frozen by being plunched into liquid ethane and subsequently cooled down further to approximately -174°C. The grid was then moved to the Cryo transporter system and mounted in the Gatan cryoholder (FEI, Hillsboro, USA). The sample was observed with a Tecnai G2 200 kV with a 4x4k CCD eagle camera, both (FEI, Hillsboro, USA). The applied voltage on applied voltage on a LaB6 source was 200 kV. Size analysis of the TEM pictures was performed by manual measurement over Gimp. Lamellarity measurements was done by manual counting uni- and multilamellar polymersomes at several images per sample with a reasonable amount of polymersomes.

FF-TEM FF was performed on a MED020 with EM VCT100 shuttle attached (Leica, Wetzlar, Germany). 1.2 μl of 25 mg/ml PB_{33}-PEO_{18} polymersomes in tris buffer was injected into a 3 mm aluminium sample carrier at the side with 300 μm depth. Afterwards, another one was placed on top with the 200 μm depth side, but care had to be taken to avoid air bubbles in between. This sandwich was then plunged into liquid ethane for 20 s and then immediately in liquid N_2. The sample carrier was afterwards fixed at the sample holder and introduced in a high vacuum chamber ($2{\cdot}10^{-6}$ mbar) at -140°C. After the lower sample carrier had been removed, the sample was coated at the same temperature with 2nm carbon, afterwards by 4 nm platinum with 45° tilted and finally with a 19 nm carbon protection layer without tilt. Outside of the chamber, the carrier was thawed for 5 min at RT, whereafter it was carefully placed at 45° angle into a 200 μl bath of tris buffer with 100 mg/ml OG for 5 min for solubilizing the polymersomes. Finally, the removed replica or single pieces of it were placed on uncoated 400 mesh copper grid that were as well carefully placed in the bath at 45°. The grid was observed in the same way, as described in the TEM analysis section. Size analysis of the TEM pictures was performed by manual measurement over Gimp, using a correction factor of $4/\pi$ to balance out the diameter error when the fracturing is not in equatorial plane[64].

SEM PB_{33}-PEO_{18} polymersomes in tris buffer with concentrations 25 mg/ml, 2.5 mg/ml and 0.25 mg/ml, respectively, were dropped on a SEM holder with carbon tape on and left overnight for air drying.were dropped on a SEM holder with carbon tape on and left overnight for air drying.The holder was then placed in a Quanta FEG 3D SEM (Philips, Amsterdam, Netherlands) with 5 kV electrons, spot size 1 and 30 μm objective lense aperture. Size analysis of the SEM pictures was performed by manual measurement over Gimp.

FF-Cryo-SEM FF was performed on a MED020 with EM VCT100 shuttle attached (Leica, Wetzlar, Germany). 1.2 μl of 25 mg/ml PB_{33}-PEO_{18} polymersome in tris buffer was injected into a 3 mm aluminium sample carrier at the side with 300 μm depth. Another one was placed on top with the 200 μm depth side. This sandwich was then plunged into liquid ethane for 20 s and then immediately in liquid N_2. The sample carrier was afterwards fixed at the sample holder and introduced in a high vacuum chamber ($2{\cdot}10^{-6}$ mbar) at -110°C. After the lower sample carrier had been removed, the sample was left for sublimation at -110°C for 1 min. The sample was subsequently coated at the same temperature with 8 nm platinum with 45° tilted and finally with a 19 nm carbon protection layer without tilting. The transfer chamber was then mounted at the cooling stage of the Quanta FEG 3D SEM (Philips, Amsterdam, Netherlands) and introduced in the vacuum chamber. The SEM was operated as described in the SEM analysis section. Size analysis of the SEM pictures was performed by manual measurement via Gimp, using a correction factor of $4/\pi$[64]. Lamellarity measurements were done by manual counting uni- and multilamellar polymersomes on at least three images per sample with a reasonable amount of polymersomes.

CLSM Five micrometers of 25 mg/ml PB_{33}-PEO_{18} polymersomes in tris buffer, labelled with Coumarin 6 (Sigma-Aldrich, Brøndby, Denmark), were placed inside a Zeiss LSM 710 confocal laser scanning microscope (Carl-Zeiss, Jena, Germany) with a 63x 1.4NA oil objective. Sections of different focus area were taken, with 10 images per section. d_P was measured automatically from the LSM 710 software.

GPM Vesicles of PB_{12}-PEO_9, PB_{22}-PEO_{23}, PB_{46}-PEO_{23}, PB_{46}-PEO_{30} and DOPC were prepared either via gentle film rehydration[58] or electroformation[115]. In gentle film rehydration, 10 mg/ml amphiphiles in $CHCl_3$ and glucose from a 1 mg/ml stock in methanol at a molar ratio of 1:1 as well as 16 μl Laurdan (Invitrogen, Carlsbad, USA) were injected in glass vial. The sample was dehydrated using blow-drying with nitrogen flow that a film appeared on the glass wall and dried on vacuum for 3-12 h. MilliQ water was added carefully to the sample without shaking the sample. The solution was left for 12 h in the dark at RT. Electroformation was done in a VesiclePrepPro chamber (Nanoion, Munich, Germany). Ten mg/ml amphiphiles in $CHCl_3$ and Laurdan were dehydrated on a indium tin oxide (ITO) coated glass slide for 1 h at RT. A greased o-ring was put around the dehydrated spot. MilliQ water was injected into the space in order to give a final amphiphile concentration of 0.1 mg/ml. Another ITO coated slide was placed onto the ring with care not to produce air bubbles. The Vesi-

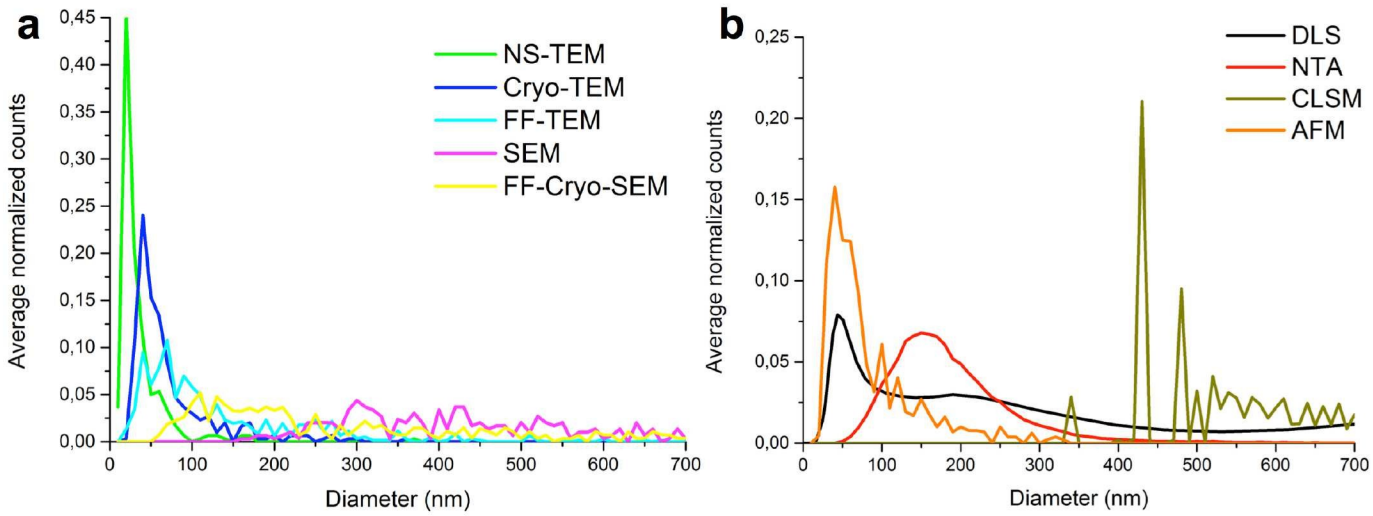

Fig. 3 Particle distribution vs diameter of a) EM-related techniques, b) the other techniques used in the study, averaged from measurements of three independent samples per technique. Most techniques revealed polymersome diameters (d_Ps) between 0 and 300 nm, where a smaller peak could be observed between 400 and 600 nm. DLS appeared more smooth, because it is based on algorithm not on number-averaged and nanoparticle tracking analysis (NTA) had a smoother curve due to a higher number of particles analyzed automatically. AFM, Cryo-TEM and Freeze fracture (FF)-TEM were close together, whereas negative staining (NS)-TEM had a shift towards smaller d_P and NTA, DLS and FF-Cryo-scanning electron microscopy (SEM) towards higher d_P. Between 400 and 500 nm confocal laser scanning microscopy (CLSM), FF-Cryo-SEM and SEM revealed similar local maxima.

clePrepPro chamber was then closed and connected to the station. Vesicles were formed at 3 V, 5 Hz over a period of 2 h at 36 ° C. The formed vesicle were put in a Eppendorf tube without exposure to light.

Vesicles were observed with a Varian Cary eclipse fluorescence spectrometer (Varian, Palo Alto, USA) with excitation wavelength of 380 nm and emission recorded in the range of 400-700 nm. Pictures were taken at 40x magnification with spectrometer-supporting software AxioVision. Picture processing and GP analysis of Laurdan were performed with ImageJ (NHI, Bethesda, USA) [58].

AFM Ten microliters of 0.25 mg/ml PB_{33}-PEO_{18} polymersomes in tris buffer were dropped on a piece of silicon wafer (Topsil, Poland, 1x1 cm^2, p-doped, single sided polish) precoated with N-(6-Aminohexyl)aminopropyltrimethoxysilane (92%, AB110807, abcr gmbh, Karlsruhe, Germany). After 1 min of absorption of the vesicle on the support, about 500 μl of MilliQ water was dropped using a pasteur pipette. Using a tissue, the liquid was absorbed. The procedure was repeated three times. After the last washing step, the silicon wafer was blown dried with air and directly placed in a XE-150 AFM (Park Systems, Suwon, South Korea). Polymersomes were imaged in non-contact tapping mode using the AFM system. The acquisition program was XEP 1.7.70 (Park Systems, Suwon, South Korea). The image size was 5x5 μm^2 with a resolution of 256x256 pixel. The AFM probe (Tap300Al-G, BudgetSensors, Sofia, Bulgaria) had a force constant of 40 N/m, a tip radius of 10 nm and a resonance frequency of 300 kHz. The images were leveled in x- and y-direction and d_P was obtained using the threshold method available in the analysis software XEI 1.8.0 (Park Systems, Suwon, South Korea).

Micropipette aspiration Some drops of approximately 0.25 mg/ml PB_{33}-PEO_{18} polymersomes in tris buffer were injected in a glass specimen chamber. Observation was performed using an Axioconvert 100 (Carl Zeiss, Jena, Germany) with 100x magnification of oil immersion objective. A micropipette with approximately 1.9 μm inner diameter was introduced in the specimen chamber, whereafter a polymersome (d_P 2.5-3 μm) was soaked by the suction pressure controlled pipette. During the micropipette manipulation experiment, live-images with CCD camera (DAGE-MIT, Michigan City, USA) and pressure with pressure transducer (Validyne Engineering, Northridge, Canada) were monitored & recorded on a computer by using a LabVIEW program. The elastic modulus properties, elastic-area compressibility modulus K_a and the bending elasticity modulus k_c were calculated from the geometrical shape of the micropipette inner diameter, diameter of the spherical segment of the polymersomes exterior to the pipette and projection length [80,116,117].

LDE Zeta potential measurements were performed using the Zetasizer (Malvern, Worcestershire, UK). One milliliter of 25 mg/ml PB_{33}-PEO_{18} polymersomes in tris buffer were injected in a zeta potential cuvette carefully to avoid air bubbles. The number of runs, depending on the quality of the results, varied between 20 and 100. All measurements were done at 25°C.

3 Results & Discussion

Size

Size analysis was performed with DLS, NTA, TEM, NS-TEM, Cryo-TEM, FF-TEM, SEM, FF-Cryo-SEM, CLSM and AFM. Distributions of d_P from EM-related techniques are shown in Figure 3a, while results from the other techniques are depicted in Figure 3b. Most

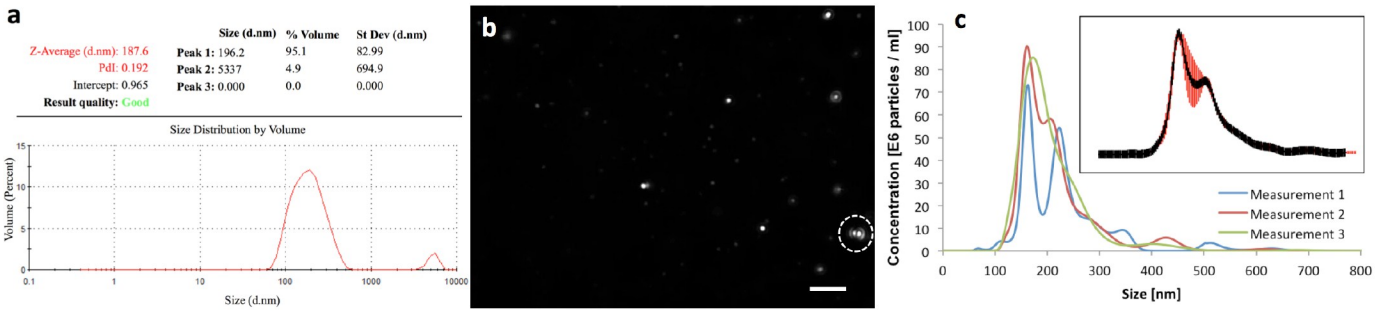

Fig. 4 DLS & NTA analysis: a) Representative scheme of DLS measurement. Z_D (here referred as Z-average) and PDI_{DLS} on the right (here referred as PdI) are calculated using cumulant analysis, where peak statistics on the left and in the diagram below are based on NNLS. b) Screenshot of video record of NTA analysis with PB_{33}-PEO_{18} polymersomes with a concentration of 0.025 mg/ml. It is crucial to obtain a balance in the camera exposure time, between too high, producing diffraction rings as seen on the right side[38] and too low that smaller polymersomes will be left out. Scale bar is 200 μm. c) Size vs concentration of 0.025 mg/ml PB_{33}-PEO_{18} polymersomes analyzed with NTA. The main d_Ps were in the range from 150 to 300 nm, where there were small peaks also between 400 and 600 nm. The differences between the measurements mirrors the polydispersity of the sample. The sharp peak of the first measurement (blue) could be due to automatic finite track length adjustment (FTLA). Inset: Concentration distribution over diameter.

d_P measurements are in the range of 0 to 300 nm, whereas there are two peaks between 400 and 500 nm for the CLSM measurements. Small peaks in the 100-300 nm d_P range are observed with AFM, Cryo-TEM and FF-TEM. With NTA, DLS and FF-Cryo-SEM the highest peaks are in the range between 150-250 nm and for NS-TEM the highest peak was below 50 nm.

The size distribution for DLS was performed with the focus on minimizing the known drawback of DLS size analysis i.e. the bias towards few larger aggregates or polymersomes as these scatter significantly more. The original intensity size distribution curve based of the Rayleigh scattering intensity was converted to volume size distribution. The intensity of Rayleigh scattering I has a relationship to the particle diameter d of $I \sim d^6$, meaning that a particle of 1000 nm diameter will scatter one million times more than a particle of 100 nm diameter. Volume size distribution takes Mie scattering into account, where the relation between diameter and scattering intensity is more realistic[118]. A further drawback of DLS is related to how the algorithm used to extract size (diameter) information deals with polydisperse samples. The usual algorithm for obtaining the intensity-weighted hydrodynamic d_P (Z-average size or Z_D) and the polymersome polydispersity index ($PDI_{DLS} = \frac{\delta^2}{Z_D^2}$, where σ is the distribution width of d_P[119]), is cumulant analysis. However for PDI_{DLS} above 0.25, the non-negatively constrained least squares (NNLS) should be applied according the manufacturers recommendations. This algorithm provides higher correction, stabilizing and weighting factors that, when combined, can extract more information out of the scattering intensity than the cumulant algorithm[120]. Both algorithms are visualized in Figure 4a with Z-average and PDI_{DLS}, stated as PdI, derived from cumulant analysis, at the right side and the peak statistics, derived from NNLS on the left side and plotted in the diagram below. Since PDI_{DLS} values larger than 0.25 can be expected for PB-PEO polymersomes prepared with film rehydration, we used volume size distribution values, derived from NNLS. Even though the first distribution peak at about 80nm d_P was in accord with several other analysis techniques like Cryo-TEM or AFM, two more broad peaks at 1500 nm and 5000 nm were observed (not shown). Although we used an algorithm which should minimize the bias towards larger polymersomes, it seemed that DLS was still not capable of giving a realistic size distribution of polydisperse samples.

NTA revealed one single broad peak with a maximum around 150 nm. This diameter is larger compared to the prevalent diameters coming out of the other techniques with the exception of CLSM. In contrast to DLS, NTA tracks single-particle and therefore has a number-averaged size distribution, based on a significantly higher number of polymersomes than with any other of the studied techniques. According to the NTA experiment report, approximately a mean number of 126 polymersomes per frame were measured. With an assumed mean polymersome presence of 0.5 s in the laser spot (which is a reasonable assumption when watching the observation video, which can be found in the supplementary information), 1800 frames per video and three videos per sample, a total of 136000 polymersomes were identified and analyzed. This is 12 times larger than for the CLSM analysis and 1360 times larger than the manual measurements.

However, several error sources are hidden in the interplay between the scattered light projections and the camera aperture. On the one hand, a larger aperture, integrates scattered light projections of polymersomes of all d_P but could lead to oversaturation of the CCD camera due to the scattered light projection of the larger polymersomes. On the other hand, when using a lower aperture there is an increased risk of overseeing poorly scattered light projections from small polymersomes. Oversaturation of the camera leads to blurry projection and tracking errors (see Figure 4b dotted circle and supplementary information). This can result in an underestimation of the number of smaller polymersomes, as noted by van der Pol[53]. Additionally, oversaturated scattered light projections of polymersome aggregates can erroneously be classified as one large polymersome. Another error source is the minimum track length, meaning the minimum number of frames, in which a polymersome is present. If the threshold for this length

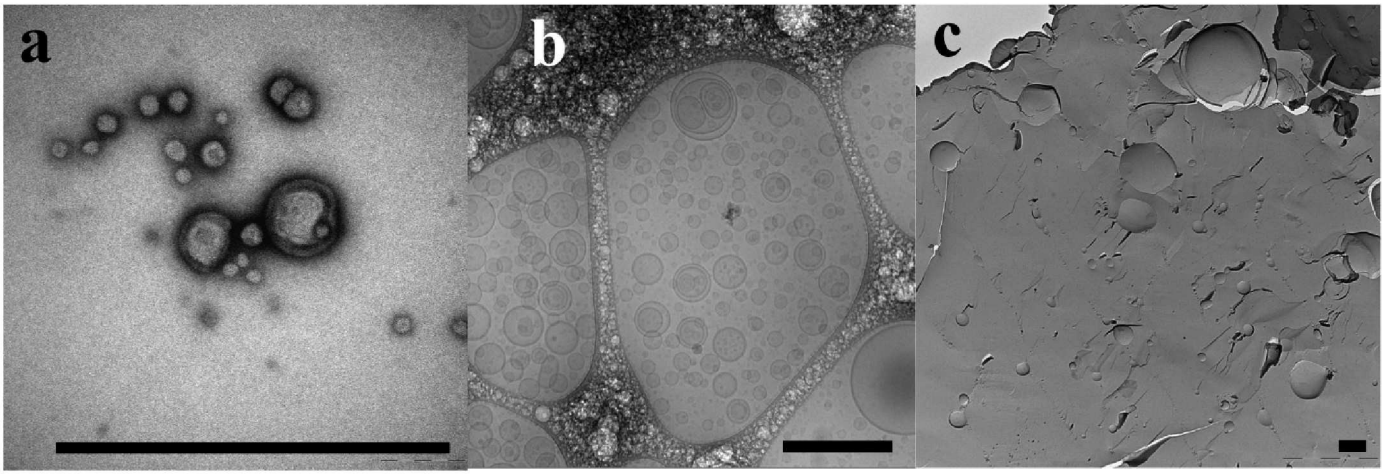

Fig. 5 NS-TEM, Cryo-TEM and FF-TEM analysis: TEM images of PB_{33}-PEO_{18}, prepared by a) NS-TEM, b) Cryo-TEM and c) FF-TEM. NS-TEM revealed mainly small and middle-sized polymersomes whereas polymersomes in a broad size range was visible with Cryo-TEM and FF-TEM. A high degree of multilamellarity is apparent in the Cryo-TEM image. Scale bar is 400 nm.

is set too high, small polymersomes are excluded, if it set too low, the sizing accuracy of individual polymersomes is reduced[38]. Automatic adjustment of the track length (finite track length adjustment, FTLA) can result in reliable diameter determination[38], but for vesicles it can lead to undesirable narrowing of peak sizes[53]. Therefore, care has to be taken when analyzing sharp peaks after using FTLA (Figure 4c measurement 1). A third reason of a bias towards larger polymersomes could be that Brownian motion is in x, y and z-direction, however the camera only detects movement in the x- and y-plane. The z-directed movement of polymersomes could therefore be observed as artificially slow, leading to artificially greater d_P[54]. DLS that also measures over time, has the same error source. In the higher d_P range between 400 and 600 nm, a small peak could be observed in the reports of the single samples 4c, which is consistent with the results from the CLSM measurements. In the Figure 3b overview scheme, these peaks are not visible anymore due to their minimal contribution to the whole distribution compared to the smaller polymersomes. This did not occur in the case of the CLSM analysis, due to the diffraction limit-related cut-off of polymersomes with smaller d_P than 200 nm.

Simple TEM without staining or freezing did not result in visible PB_{33}-PEO_{18} polymersomes, even though this process was successfully applied, using polymersomes of other chemistries like polystyrene polyacrylic acid (PS-PAA)[121]. In previous experiments with PB_{12}-PEO_9, prepared by detergent-mediated film rehydration, polymersomes could be visualized directly with TEM. However for these vesicles, only empty grid were observed.

When observed with NS-TEM, polymersomes were visible on the grids. The majority was intact, as can be seen in Figure 5a however some of them appeared ruptured and deflated. In contrast, PB_{12}-PEO_9 vesicles appeared mainly in collapsed form[52]. This could be due to the smaller polymer M_w or the staining agent (phosphotungstic acid versus uranyl formate used in[52]). There were less polymersomes observed in the NS-TEM images compared to FF-TEM, Cryo-TEM or FF-Cryo-SEM due to the higher dilution, chosen since higher concentrations would break the holey carbon film of the TEM grid. In the size overview in Figure 3a+b, NS-TEM analyzed polymersomes had d_P values about 20nm less than for polymersomes analyzed with AFM, Cryo-TEM and FF-TEM. The main reason behind this decrease was most probably osmotic shrinkage due to phosphotungstic acid, which will have a higher osmotic activity than the tris buffer in the polymersome lumen due to higher ion concentration. Large polymersomes (> 300 nm) were not polymersomes showed d_p values about 20 nm smallerobserved. This could be due to chance, as far as only regions of the whole grid were observed. However, different regions were observed per sample, so the chance of missing out larger polymersomes (which could be observed with other EM techniques and CLSM) was low. On the other hand, larger polymersomes would be less stable towards osmotic shrinkage due to staining and drying involved in the NS-TEM sample preparation. This argument is consistent with the occasional observation of polymer bilayer membrane fractions that were found on some images (see supplementary information).

Cryo-TEM revealed polymersome d_Ps in the range from below 10 nm up to almost microns, including highly multilamellar ones (see Figure 5b and supplementary information). The samples were highly heterogeneous, even within individual samples local accumulations of small and large polymersomes could be observed (see supplementary information). As shown in Figure 3a, the majority of polymersome d_Ps were around 50 nm, though some polymersomes of d_P between 200 and 400 nm could be observed.

The plunge-freezing of the polymersomes can be seen as taking a "snapshot" of the polymersomes in their native state. Due to the fact that the freezing rate of liquid ethane is quite high (12000 K/s[122]), freezing artifacts can be assumed to be negligibly small. For small and monodisperse samples, this technique can enable an undistorted direct imaging and quantification of

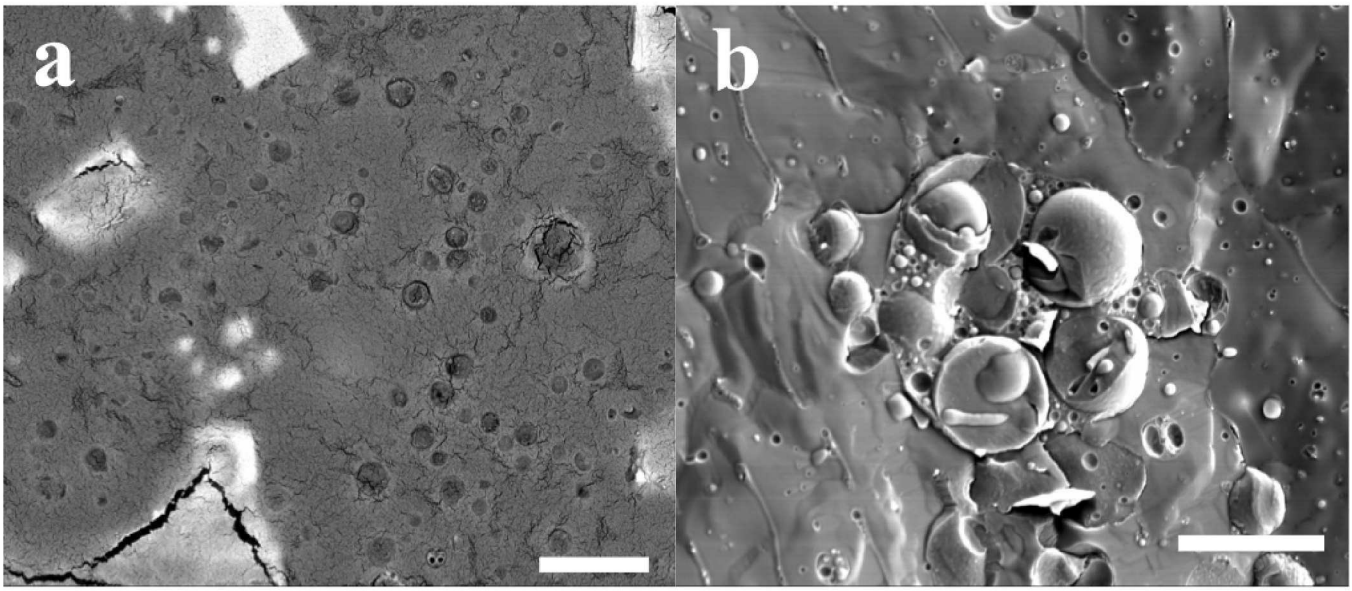

Fig. 6 SEM & FF-Cryo-SEM analysis: SEM images of PB_{33}-PEO_{18}, prepared by a) SEM and b) FF-Cryo-SEM. SEM preparation only revealed completely deflated and dehydrated polymersome shells at larger d_P, whereas with FF-Cryo-SEM, lots of multivesicular polymersomes could be obtained. Scale bar is 3 μm

the particle diameter, leading to realistic number-weighted size distributions, as stated by Egelhaaf[111]. For larger particles such as polymersomes, deformation effects could occur due to thickness fluctuations in the vitrified water layer. This layer is thinner towards the middle of a hole in a carbon holey grid. These thickness fluctuations could be of the same order of magnitude as the polymersome d_P, resulting in overestimation or underestimation of d_P[111]. For mainly larger polymersomes ($d_P > 500$ nm), photon-mediated techniques like CLSM would therefore be the more suitable analysis technique. In contrast to NS-TEM, staining or drying steps are involved in the Cryo-TEM preparation that could destabilize larger polymersomes. For this reason and due to the higher concentration compared to NS-TEM discussed before, larger polymersomes could be observed, as can be seen in the supplementary information.

During FF-TEM, the freeze-captured polymersomes were fractured and coated, where the replica from this coating is observed, separated from the original polymersomes. The great advantage of FF-TEM over Cryo-TEM is the three-dimensional appearance of the micrographs, making it desirable for polymersome surface structure research with higher resolution than what can be obtained with FF-Cryo-SEM. The sample can also be observed at any time after preparation, whereas for Cryo-TEM samples should be observed directly afterwards and always be maintained at cryogenic temperatures. Even so there is still a risk of melting the samples under the electron beam, thus observation time can be limited. A disadvantage with FF-TEM is the need for separation of the thawed polymersomes from their carbon-platinum copy. Even with minimal agitation and highest possible lateral stability the replica is prone to damage during solubilization of the polymersomes in detergent. Additional forces are applied when the replica is removed from the detergent solution and dried on a copper grid. The weakest point of the replica is the polymersome fracture plane[123], thus if replicas break, they usually break at the edge of larger polymersomes, as can be seen in Figure 5c or in areas of high polymersome accumulation (see supplementary information). This could lead to an underestimation of the number of larger polymersomes, compared to FF-Cryo-SEM that showed significantly more polymersomes above d_P of 400 nm, even though the preparation in terms of freeze fracturing was the same. An additional drawback for size analysis with both methods is that the fracture plane is not going through the equatorial plane of the polymersome. Two studies from Coldren et al. and Egelhaaf et al. have addressed this problem and made several suggestions for how to align FF-TEM and Cryo-TEM size distribution analyses[64,111]. Coldren et al. found a correction factor of $4/\pi$, which we applied here. However, both studies were performed on monodisperse liposome or surfactant vesicles and Egelhaaf et al. reported an effect on the observed d_P depending on polydispersity[111]. They furthermore found an underrepresentation of small liposomes due to the higher probability of larger liposomes to get fractured and due to invisibly small caps or cavities from small liposomes. This could explain the lower number of polymersome with d_P 30-50 nm compared to NS-TEM and Cryo-TEM in Figure 3a. For polydisperse samples Egelhaaf recommends a larger amount of analyzed vesicles[111]. Thus, if more than the 300 polymersomes had been analyzed, the size distribution may have become more similar to the measured size distribution of Cryo-TEM. Automatic imaging software (e.g. ImageJ or similar programs) would be challenged by the low contrast between polymersomes and background, and manual analysis may be required to get good statistics.

Regarding SEM, we analyzed two preparation approaches: one based on simple dropping of polymersomes onto a SEM holder

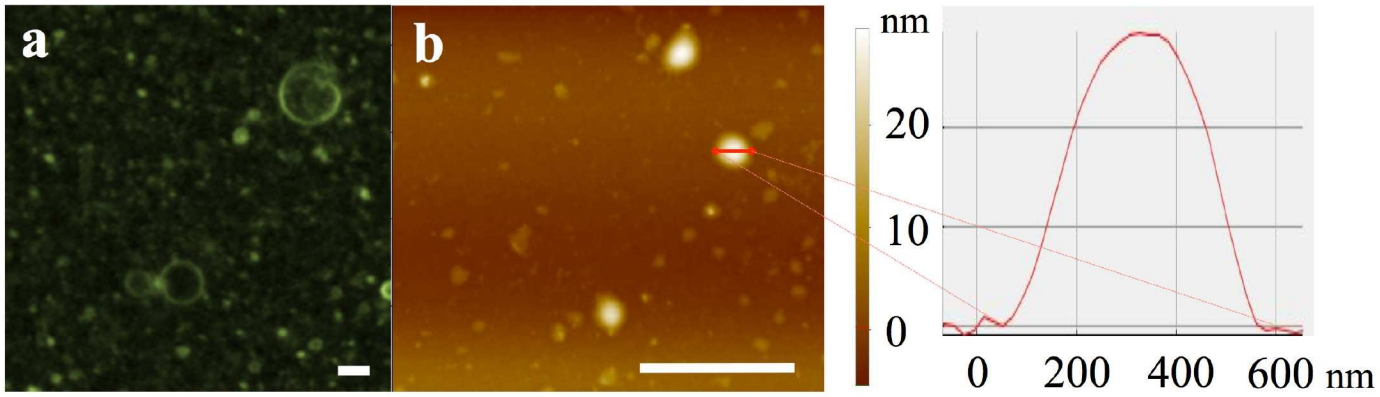

Fig. 7 CLSM & AFM analysis: a) CLSM images and b) AFM topographic images of PB_{33}-PEO_{18} polymersomes. CLSM analysis showed mainly polymersomes visualized with the bilayer labeling fluorophore coumarin 6 and only a few larger polymersomes, where the lumen and the bilayer cross section could be visualized. AFM visualized polymersomes were mainly spherical and some possibly multilamellar (see middle-left side of panel b). Scale bar is 2μm.

with air-drying and subsequent observation, and another using freeze-fracturing as in FF-TEM but with observation of the coated sample directly instead of observing the separated replica (FF-Cryo-SEM). The first approach gave surprisingly good agreement for polymersomes with $d_P > 400$ nm, as shown in Figure 3a. However for $d_P < 400$ nm, the majority of polymersomes had d_Ps where no other size measurement technique had any significant d_P peaks. Upon inspection dehydrated cavities of polymersome shells were observed (Figure 6a) and for large polymersomes there was enough material to deform the underlying carbon tape on the SEM holder, whereas for smaller polymersomes this was not possible, thus they remained invisible.

The size distribution of FF-Cryo-SEM was significantly shifted towards larger polymersomes compared to Cryo-TEM and AFM, less shifted compared to FF-TEM and in good agreement with NTA analysis. This could be related to the resolution limit, which was not 2 nm in all images for analysis[67]. Higher magnification resulted in a higher electron density per area and the samples started to melt above 25000x magnifications. At 50000x magnification, it was difficult to focus due to the rapid melting and cracks appearing on the surface (see the supplementary information). Polymersomes with $d_P < 200$ nm were hardly visible at lower non-invasive magnification, similar to the observations with NTA, where scattering intensity was too low. NTA and FF-Cryo-SEM could therefore be ideal size analysis tools for filling the d_P gap between Cryo-TEM, FF-TEM or AFM on the one side (where size limitation for micron-sized polymersomes could occur due to deformation effects at Cryo-TEM or AFM and replica fragilities at FF-TEM) and photon-mediated techniques on the other side, where size limitation for polymersomes with $d_P < 200$ nm could occur due to the diffraction limit.

Images of FF-Cryo-SEM revealed high amounts of multivesicular and a few multilamellar polymersomes, as can be seen in Figure 6b. The same correction factor used for FF-TEM was also applied at FF-Cryo-SEM, because both have the same fracture plane issue, discussed earlier. The size distribution of FF-Cryo-SEM was shifted towards higher d_P due to the resolution limit mentioned before but also due to the fragility of the replica at FF-TEM. Especially in regions with multivesicular polymersomes as in Figure 6b there were plenty of cavities where no stabilizing carbon was present at the surface[123]. Consequently, these regions broke apart and could not be visualized in the TEM anymore. Regions with lower accumulations of polymersomes that usually contained fewer large, multilamellar or -vesicular polymersomes (see supplementary information) provided a more even surface and thus a higher lateral stability of the replica. Those regions were dominant at FF-TEM, whereas at FF-Cryo-SEM, regions with high and low polymersome accumulation were equally distributed.

Of the methods tested, CLSM was the only direct visualization method that allowed observation in completely undisturbed native environment. CLSM revealed Coumarin 6-labelled polymersomes, where the Coumarin 6 mainly filled the surface completely at the smaller polymersomes, however the lumen could be seen for a few larger polymersomes or tubular structures, visible in Figure 7a (further images and a video can be found in the supplementary information). There were few polymersomes with approximately d_P of 330 nm, two peaks between d_P of 400 and 500 nm, and a few polymersomes with d_P between 500 and 2000 nm. The ones above d_P 700 nm were not shown in Figure 3b for clarity purposes. The two peaks between d_P of 400 and 500 nm were in good agreement with the results of the SEM analysis and in reasonable agreement with the FF-TEM and FF-Cryo-SEM analyses. This suggests that the polymersomes did not alter shape during rapid freezing or even air drying above d_P of 400 nm, and that the $\pi/4$ correction factor could be applied for polymersomes with $d_P > 400$ nm. The size histogram analysis was with a bin width of 10 nm (the same that was used in Figure 3). As the total number of analyzed polymersomes was larger than 11000, the size distribution can be seen as representative. No multilamellar polymersomes could be observed using CLSM, even though other techniques revealed their presence and studies reported that this would be possible[60]. The size restriction remains a challenge for this method, as for most optical measurement techniques. A

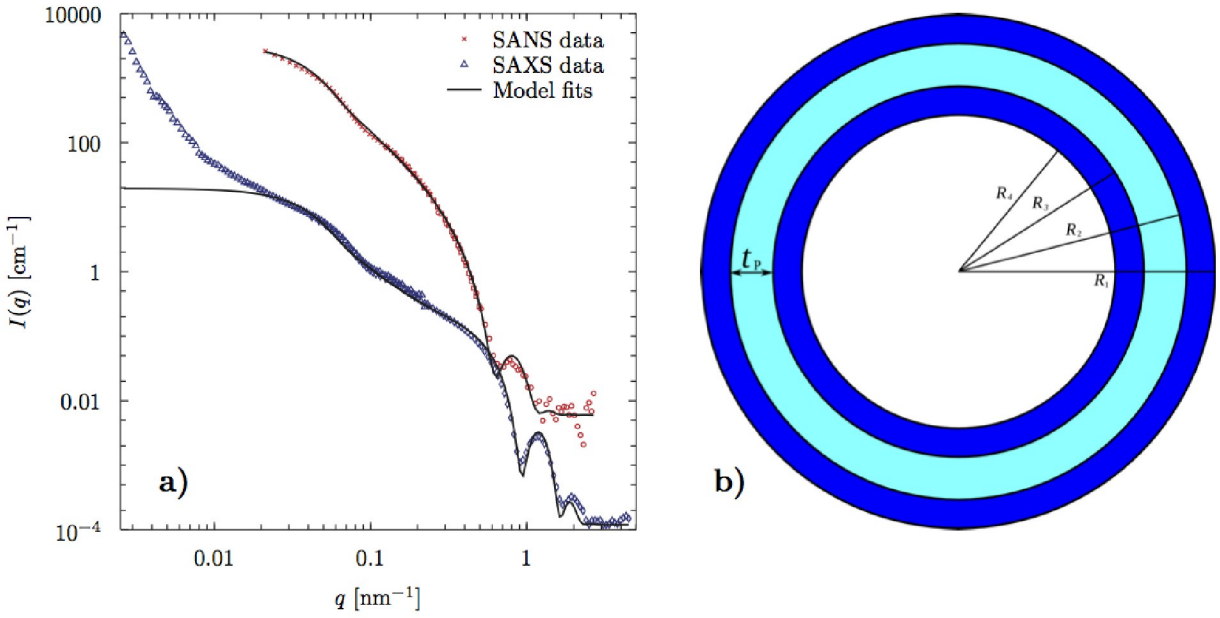

Fig. 8 a) SAXS and SANS intensities as a function of the magnitude, q, of the scattering vector on an absolute scale, i.e. intensities are given as scattering cross-section per sample volume in cm^{-1}. The quantity q is related to the scattering angle 2θ and the wavelength λ of the radiation as $q = 4\pi \sin\theta/\lambda$. b) Cross-section of SAXS/SANS model used to fit both curves.

novel approach by Kunding et al. used the fluorescence intensity of immobilized labelled vesicles to obtain vesicle diameter below 200 nm with good agreement with Cryo-TEM[61]. However the immobilisation procedure may lead to potential polymersome shape changes. Other methods like stimulated emission depletion microscopy (STED) can provide significantly sharper images below the diffraction limit, as shown in various studies on tissues[62] and polymersomes[112].

The size distribution of AFM analysis (Figure 3b) correlated well with Cryo-TEM (Figure 3a). Both analysis techniques have the highest peak at d_P 50 nm with the same peak width, but the AFM peak was significantly smaller compared to the peak obtained from Cryo-TEM analysis. For polymersomes with d_P between 100 and 150 nm, AFM analysis revealed slightly higher peaks. These latter peaks were in good agreement with results from the FF-TEM analysis. This could be due to the immobilization procedure since larger polymersomes could become deflated which result in capping structures similar to the ones obtained by FF-TEM or FF-Cryo-SEM, whereas smaller (and stiffer) polymersomes would not alter their shape upon immobilization. Force measurements could reveal more information here and this will be discussed in the next section. Each AFM measurement was performed within one hour, where the sample was thought to remain unchanged[80]. Also no sticking of amphiphiles to the cantilever was observed during the measurements in tapping-mode. Compared to FF-TEM, Ruozi et al. reported better surface information for AFM analysis with liposomes[40]. On large polymersomes, some holes in the surface were observed (see supplementary information), however for the most polymersomes, surfaces appeared smooth as visualized with FF-TEM, see Figure 7b. The holes could reflect deflated interiors of some polymersomes, or be due to cantilever-induced artifacts. AFM analysis did not reveal any information about polymersome interior (multilamellarity or multivesicularity) in contrast to what has been achieved with liposomes[113]. The contrast and contour of FF-TEM visualized polymersomes was higher than the ones visualized using AFM, which is in agreement with other studies[40]. Another possibility of AFM, which was not performed in this study, would be to analyze polymersomes in liquid mode. Here they would have been captured in natural conditions. However they need to be immobilized, which would most likely give a difference in their properties compared to when they are diffusing freely.

Table 3 Hydrophobic core thickness t_P and lamellarity of PB_{33}-PEO_{18} polymersomes obtained by different EM and scattering related analysis methods. SAXS and SANS analysis revealed a slightly higher t_P than Cryo-TEM. Cryo-TEM had 3 times more multi lamellar/vesicular polymersomes than FF-Cryo-SEM.

Method	t_P [nm]	Multilamellar/vesicular per 100 polymersomes
Cryo-TEM	6.74±1.28	10.71±4.5
FF-Cryo-SEM		3.32±0.36
SAXS & SANS	7.6±0.2	

Bilayer thickness

The only methods, where information about t_P could be obtained were Cryo-TEM, SAXS and SANS. The t_P values of PB_{33}-PEO_{18} polymersomes obtained using these three techniques, are summarized in Table 3. They agree with t_P values found for PB-PEO from other studies[124,44]. Cryo-TEM has shown to be a powerful tool for obtaining t_P[125]. The reliability of t_P measurement by Cryo-TEM however depends on d_P. t_P in Cryo-TEM images is visualized as the difference in electron scattering intensity of the bilayer compared to the aqueous background[64]. Near the equa-

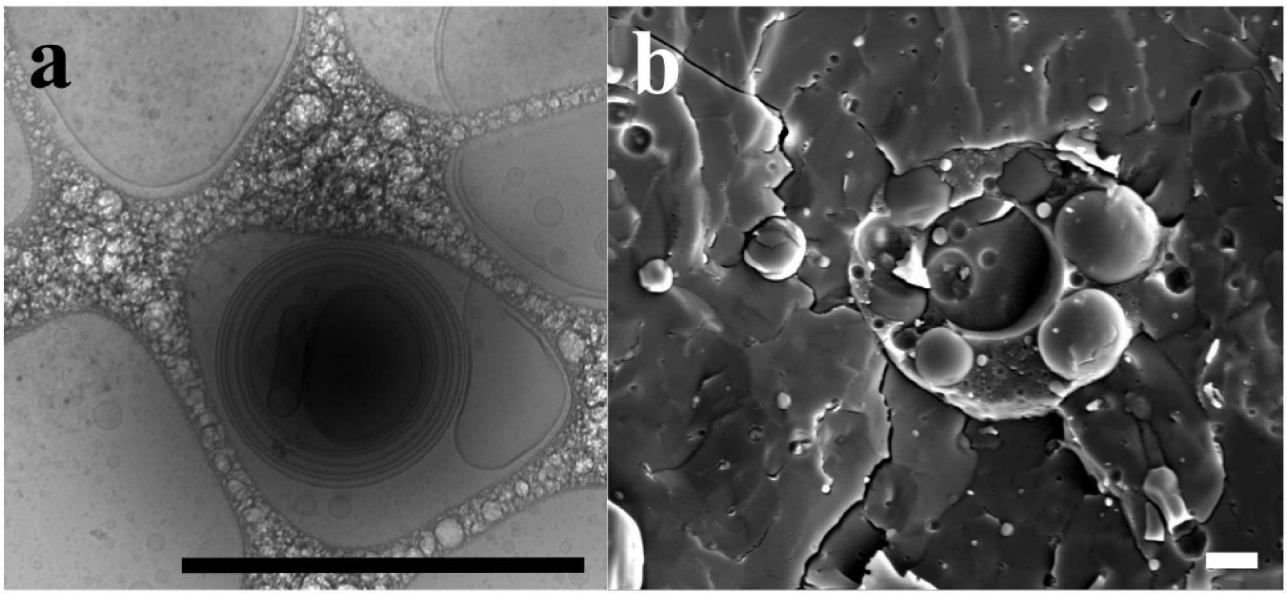

Fig. 9 Cryo-TEM & FF-Cryo-SEM analysis: a) Typical Cryo-TEM image revealing mainly multilamellar polymersomes, where at FF-Cryo-SEM, multivesicular polymersomes could be seen more often (b). Scale bar is 1μm.

torial plane of the polymersome, the electron beam enters the bilayer in a very small angle. Consequently, the electrons have to pass a long distance through the bilayer, lowering the contrast and the certainty of t_P. At the interior polymersome edge, this effect is more pronounced than at the exterior edge. Furthermore, this effect has a higher influence with smaller polymersomes, where the t_P is larger in comparison to d_P[64]. Thus, t_P analysis with Cryo-TEM has to be seen in the light of these limitations.

Small-angle X-ray and neutron scattering (SAXS and SANS) on the other hand usually can provide more precise information[126]. The SAXS and SANS scattering patterns, arising from particles of simple geometrical shapes, can be calculated analytically. The structural parameters of this model can then be optimized by χ^2 fitting of the calculated curve to the measured data (shown in Figure 8a). Assuming the polymersomes to be spherical and polydisperse, we analyzed the data using a multi contrast shell model with three layers. The cross-section of the model is shown in Figure 8b. The inner and outer shell, representing the PEO-chains, whereas the middle shell represents the hydrophobic core of the bilayer, containing the PB-chains. The same model is used to fit SAXS and SANS data simultaneously.

It is clear from Figure 8a) that the model does not fit the data well at very low q. This is owing to the presence of large vesicles of d_P of more than 100 nm. In the q-range from 0.2 to 2 nm^{-1}, on the other hand the fit quality is very good. In this regime length scales from 30 to 3 nm are probed, corresponding to t_P and cross-section.

The fitted parameters of the model are shown in Table 4. The thickness of a PEO monolayer could not be unambiguously determined and was fixed at the reasonable value of 1.8 nm corresponding to two radii of gyration of a free PEO_{18}-chain in solution. Further details of the model can be found in the supplementary information.

Table 4 Relevant parameters of SAXS/SANS modeling.

Fit parameter	Value
Mean polymersomes radius R_P	29.6±0.5nm
Gaussian width of R_P distribution	12.0±0.2nm
Thickness of PB_{33} bilayer, t_P	7.6±0.2nm
Thickness of PEO_{18} monolayer	1.81nm (FIXED)
Width of polymersome interface s	0.73±0.03nm
Deduced parameters	**Value**
Volume fraction of water in PEO shells	0.34
Interface area per block copolymer	0.87nm^2

t_P values determined from SAXS/SANS modeling is in good agreement with theoretical estimates[127]. However it has to be taken into account that the preparation method of the samples for SAXS/SANS involved an additional dialysis step compared to the samples for Cryo-TEM. Thus, the bilayer could be stabilized[52] and therewith become thicker during dialysis as pretreatment to SAXS/SANS analysis. In some of our previous SAXS measurements (not published), we found that the polymersome bilayer smoothes out with dialysis treatment. This could potentially result in a change in t_P due to molecular rearrangement and stretching of the block copolymers in the bilayer. We observed the same during NS-TEM observations[52].

Lamellarity

Cryo-TEM analysis gave a mean value of 10.71±4.5 multilamellar or -vesicular polymersomes per 100 polymersomes, which was three times higher than the amount observed by FF-Cryo-SEM (see Table 3). Interestingly, the amount of observed multivesicular polymersomes was higher in FF-Cryo-SEM, whereas there were more multilamellar polymersomes observed

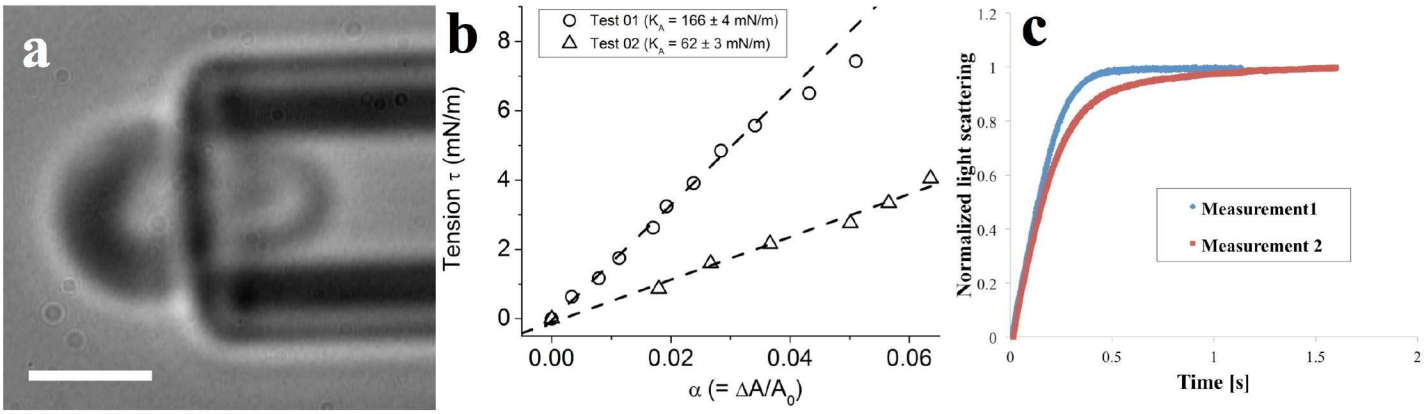

Fig. 10 Micropipette aspiration & Stopped-flow light scattering (SFLS): a) Micrograph image of micropipette aspiration setup. PB_{33}-PEO_{18} polymersomes attach to the micropipette due to capillary forces and can be aspired partly into the pipette by application of negative pressure allowing for determination of bending elasticity modus k_c and elastic-area compressibility modus K_a. Scale bar is 1μm. b) The direct area expansion plot with tension increasing. The plots shows after subtracting out the initial soft-exponential rise of tension, which is known as k_c. c) Scattering intensity vs time for SFLS measurement of PB_{33}-PEO_{18} polymersomes. An exponential increase in scattered light reflects polymersome shrinkage due to rapidly established osmotic gradients driving water out of the polymersomes. After approximately 1 s, d_P reached a new equilibrium value.

using Cryo-TEM (Figure 9 and supplementary information). Cryo-TEM is more likely to show the real distribution, because the interior of the polymersome is always revealed, allowing for identification of both structures. The higher number of multilamellar structures could be due to the film rehydration procedure, where their formation is more likely[128]. The higher appearance of multivesicular polymersomes at FF-Cryo-SEM is consistent with these structures being more prone to fracturing than multilamellar polymersomes. In FF-Cryo-SEM structures that can be fractured easier are more likely to be observed. The interior forces are also more homogeneously distributed in multilamellar polymersomes, whereas in multivesicular polymersomes the uneven distribution of polydisperse polymersomes result in heterogeneous force distributions, all weakening the outer bilayer. SAXS and SANS showed an unilamellar behaviour due to prior extrusion preparation. They would otherwise be powerful tools to show multilamellar polymersomes.

Elastic properties

The two elastic moduli, k_c and K_a were analyzed by micropipette aspiration (Figure 10a and video in the supplementary information) following a procedure after Evans[116,117,129]. The fractional surface area change ($\alpha = \Delta A/A_0$) polymersomes with increasing suction pressure was monitored by camera. The isotropic tension change of the polymersome surface τ was calculated from the geometrial shape of the polymersomes under applied pressure, as described elsewhere[80]. The linear slope from α against τ plot yielded a K_a of 60-170 mN/m, see Figure 10b. No k_c could be obtained due to the small d_P. K_a was significantly different from studies for PB-PEO polymersomes by Dimova (K_a 470±15 mN/m[79]). However, Dimova et al. used a different preparation procedure, including sucrose in the buffer. Sucrose has a significant effect on the self-assembly behavior of polymersomes and thereby also on the elastic properties of their bilayers. PB_{12}-PEO_{19} polymersomes are only forming if sucrose is present in the solution, otherwise they assemble to worm- or spermlike structures[52]. They obtained polymersomes with a mean d_P of 15 μm, whereas polymersomes of this work did seldom exceed 1 μm d_P. In general, k_c is reflecting thermal undulations and the soft regime of area compliance. The initial soft-exponential rise with area expansion in Figure 10b reveals smoothing of thermal shape fluctuations[117]. K_a had a large variety most likely due to the differences in preparation compared to the work of Dimova et al.[79]. A video showing the micropipette aspiration of a single polymersome is given in the supplementary information.

Permeability

For shrinking/swelling studies polymersomes must be extruded and we analyzed PB_{33}-PEO_{18} polymersomes based on extrusion to a nominal d_P of 200nm. SFLS revealed a polymersome permeability of 5.87±0.31 μm/s, which is in the range of permeabilities, obtained by other studies on PB-PEO polymersomes (3.1±1.6 μm/s,[130]) and lower than what has been obtained with phosphatidylcholine liposomes (10-150 μm/s,[131]), see Figure 10c. In previous experiments, we measured PB_{12}-PEO_9, PB_{22}-PEO_{23}, PB_{35}-PEO_{14}, PB_{46}-PEO_{23}, PB_{46}-PEO_{30} that revealed permeabilities between 7 and 80 μm/s with an increase with increasing hydrophobic block length, except for PB_{22}-PEO_{23}. This was due to the significantly smaller d_P of the PB_{22}-PEO_{23} polymersomes. PB_{12}-PEO_9 had a five times higher permeability than second highest permeable PB_{35}-PEO_{14} (80 μm/s versus 14.5 μm/s). On a different SFLS instrument we even measured 190 μm/s for PB_{12}-PEO_9 polymersomes[52]. It seems that from a certain number of hydrophobic blocks the membrane permeability is exponentially increasing. Regarding the hydrophobic block length, PB_{33}-PEO_{18} should have a permeability close to that of PB_{35}-PEO_{14}, however it is only one third. In the polymersomes from previous experiments of our group and Kumar et al.[52] we used sucrose in the buffer as well, which has a significant influence on the bilayer as discussed before. Interestingly, for

liposomes, there is no relationship between permeability and K_a, k_c or t_P [132]. However permeability correlates to the area per lipid. Only when cholesterol was added, a linear relationship between K_a and permeability was found, probably because K_a becomes linear with area per lipid ratio [132].

Polarity

Polarity measurements are used to determine the hydrophobicity of a polymersome bilayer. This can help to deduct water or ion permeability or incorporation capability for membrane proteins. For polarity experiments, using GPM, we compared four different polymers (PB_{12}-PEO_9, PB_{22}-PEO_{23}, PB_{46}-PEO_{23}, PB_{46}-PEO_{30}) and DOPC liposomes. Laurdan labeled giant polymerosomes and liposomes were produced using GUV formation and electroformation as described in [58,133]. Further details are given in the Materials & Methods chapter. Laurdan is a polarity sensitive fluorophore located in the bilayer with its functional group polarized parallel to the hydrophobic chains of the bilayer [95]. Laurdan exhibits a red shift in spectral wavelength emission when set into polar environment or elevated temperatures [95,109]. This shift can be quantified as values ranging between -1 and 1 using the GP function [134]. All bilayers of the polymerosomes appeared bluish indicating that they are significantly more hydrophobic than DOPC liposomes which appeared green [95], see Figure 11. GPM and RGB processed images of vesicle bilayers of all polymerosomes compared to DOPC are shown in Figure 11. Laurdan labeling was distributed equally in PB_{12}-PEO_9, PB_{46}-PEO_{23} and PB_{46}-PEO_{30}, whereas it varied in PB_{22}-PEO_{23} vesicles. From the GP histogram in Figure 12 of polymerosomes and DOPC liposomes, one can recognize the red shift for DOPC liposomes and the blue shift for the polymersomes. Among the polymersomes, the blue shift increased linearly with increasing hydrophobic block length. The spectral emission shift from 22 hydrophobic units to 46 was quite small when compared to the one between 12 and 22. This could arise from the small d_P values for both PB_{46}-PEO_{23} and PB_{46}-PEO_{30} polymersomes.

Zeta potential

Zeta potential was measured using LDE on a Nano Zetasizer (Malvern, Worcestershire, UK), the same instrument that was used for DLS measurements. The measured zeta potential for PB_{33}-PEO_{18} polymersomes was 3.32±0.35 mV which indicated that polymersomes of this chemistry seemed to exhibit minimal surface charge. This is confirmed in other studies e.g [3,135,136]. The zeta potential is a measure of the electrostatic repulsion between particles. Particles with a zeta potential $>$ 30 mV or $<$ -30 mV will repel each other and thereby avoid aggregation, where they will aggregate in the intermediate range [137]. Thus, PB-PEO polymersomes are more prone to aggregation than polymersomes with a higher surface charge. As charges may be screened by the presence of ions (here due to 50 mM NaCl concentration in the buffer), the zeta potential (and potential aggregation) of polymersomes may be controlled to some extent [138].

4 Conclusion

Here we have presented 17 techniques to analyze (PB-PEO)-polymersomes and discussed them in terms of d_P, t_P, lamellarity, elastic properties, polarity and zeta potential. Advantages as well as drawbacks of each method were discussed and exemplified using specific PB-PEO polymersome samples. Although our review focus on polymersome analysis, it also pertains to liposome analysis. In summarizing the results we arrive at the following conclusions:

DLS has the advantage of being simple, fast and well-established. For highly polydisperse samples, as used in this study, it is though not suited, even though the parameters and algorithms for calculating the size distribution was optimized towards

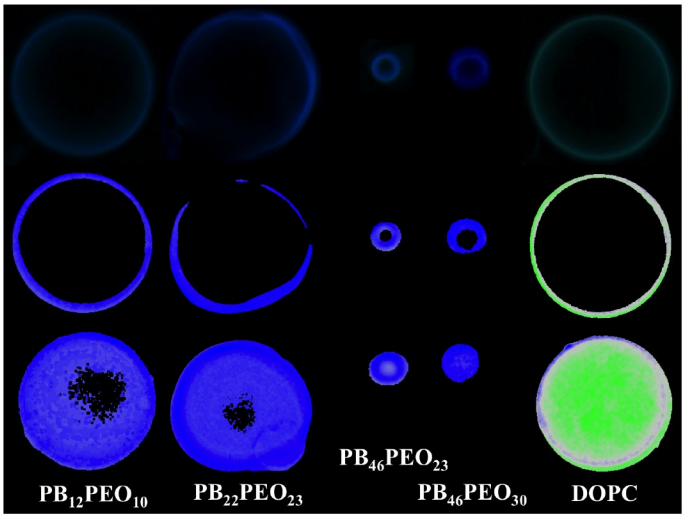

Fig. 11 Microscopy pictures of polymerosomes in equatorial plane of the vesicle upper panel), their RGB processed profile from Laurdan emission in the equatorial plane (middle panel) and in the polar plane (lower panel). Laurdan is blue-shifted on all polymersomes, where it is exhibits green emission at the 1,2-dioleoyl-*sn*-glycero-3-phosphocholine (DOPC) liposomes.

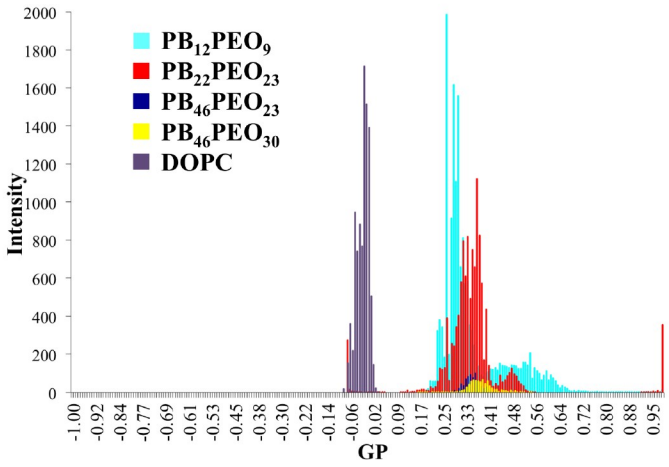

Fig. 12 Generalized polarization (GP) histogram of Laurdan spectral emission shift for all vesicles, shown in values between -1 and 1 by integrating the intensities in a Laurdan-specific GP function [134]. The spectral emission shift of Laurdan depends on the polarity of its environment. An unlinear blue shift with an increase of hydrophobic units was observed.

minimizing the bias towards larger polymersomes.

NTA can be seen as a superior fast technique compared to DLS, due to size-distributions based on number-averages, in contrast to algorithm-based averages with DLS measurements. NTA has the same easy preparation as DLS, however it faces as well the same problems as DLS, when it comes to polydisperse samples and the large difference in scattering intensity between larger and smaller polymersomes[37]. Care has to be taken with the interpretation of NTA size analysis especially for polymersomes that generally have a low refractive index[36].

For analysis focusing on vesicle morphology and size measurements, NS-TEM is the method of choice for polymersomes with $d_p < 200$nm, due to its simple preparation procedures compared to FF-TEM, Cryo-TEM and FF-Cryo-SEM. For encapsulation, NS-TEM has advantages over Cryo-TEM due to the possibility of differential staining[113]. However, results from NS-TEM analysis needs to be substantiated by data from other methods, due to osmotic shrinkage caused by the staining agent.

Cryo-TEM remains the method of choice for obtaining a reliable size distribution of polymersomes below 400nm. For d_P and lamellarity measurements, it is the most realistic imaging of all methods analyzed here, due to the "capture" of polymersomes in native environments. There are no size limitations or additional labeling steps necessary as the case with CLSM or super resolution microscopy techniques such as STED. However, for obtaining the t_P values, care has to be taken with smaller polymersomes, which may be artificially thicker due to the contrast flucuations near the equatorial plane of the polymersomes.

FF-TEM has good practical feasibility in the sense that the samples can be analyzed and stored over long time periods, in contrast to sample preparation for Cryo-TEM analyses. Also FF-TEM is well suited for analysis of membrane proteins incorporation[139]. However, if exact d_P determination are required, Cryo-TEM is superior for getting a reliable size distribution.

FF-Cryo-SEM is the method of choice for morphology and topology analysis of multivesicular (and to a less extent) multilamellar polymersomes. Due to good resolution and three dimensional projection between 50 nm and micrometer scale, it can fill the "analysis-gap" between TEM and photon-mediated visualization techniques. Also information obtained with FF-Cryo-SEM can be enhanced within NTA analysis. However, FF-Cryo-SEM has a poorer resolution compared to TEM and more rapid damaging of the sample when observing at higher magnifications.

CLSM provides reliable d_P measurements for polymersomes with $d_P > 400$ nm. For polymersomes with smaller d_Ps (i.e. < 200 nm), the technique requires novel enhancements from the super resolution family such as STED. Establishing comparative d_P studies with CLSM and EM-based methods, scattering and mechanical manipulation approaches will be a major future challenge.

AFM is a versatile fast technique for smaller polymersomes. AFM size distributions closely matches distributions achieved with Cryo-TEM. Deflation or deformation effects for polymersomes below d_P of 400 nm seems to have only little influence on the size distribution, in contrast to measurements on liposome samples. AFM gives results comparable to what can be achieved with FF-TEM. However, AFM is not well suited for analysis of polymersomes multilamellarity or multivesicularity.

SAXS and SANS provides reliable information on t_P, size and polydispersity of the polymersomes, where t_P can be measured with higher accuracy compared to TEM. However their use will always be limited by complex analytical data analysis and the need for access to large-scale radiation facilities.

Micro pipette aspiration is a great technique to obtain elastic properties of polymersomes. The downside is that it is quite time consuming in terms of manually aspirating single polymersomes. A big advantage compared to AFM is the visualization of the deformation of the entire polymersome during surface tension measurement with applied pressure that will reduce errors of measurement. AFM could use a spot of something else than the polymersome for obtaining the elastic moduli.

SFLS is an easy and quick tool for measuring permeabilities through polymersome bilayers. Depending on the instrument and the algorithm used, calculated permeabilities can be significantly different. Furthermore, monodisperse and unilamellar polymersomes are required to obtain reliable values.

Finally, LDE in combination with DLS can provide reliable information on the zeta potential of polymersomes. For PB-PEO polymersomes, the zeta potential was minimal, thus this system is prone to aggregation. Care has to be taken to the buffer solution, as ions can greatly influence the measurements.

The work presented here on polymersomes can be seen as a preparative step prior towards further processing and use of polymersomes. Thus, all the analysis methods discussed here are directly applicable in polymersome-based applications such as drug delivery systems[16], artificial cells[21] or biomimetic membrane technology[27]. In this development, the methods presented here will have to be supplemented by methods focusing on characterizing biomolecule encapsulation and protein incorporation characterization. Integration of these characterization methods constitutes an interesting challenge to be addressed in future polymersome research and associated technological developments.

5 Acknowledgements

We thank Lars Schulte and Simon Levinsen, DTU Nanotech for assistance with the polymer synthesis; Fadoua Sbai, Aquaporin A/S, for assistance with SFLS analysis; Klaus Qvortrup, Ramon Liebrechts and Thomas Braunstein, University of Copenhagen, for providing assistance with freeze fracture and CLSM and access to the freeze fracture unit, the TEM and the CLSM and Noemi Rozlosnik, DTU Nanotech for providing access to the AFM. We thank NXUS for the collection and analysis of the SAXS-data. NXUS is a pilot project enabling industrial use of large scale research facilities in collaboration with university experts in the field of neutron and X-ray science. NXUS is funded by the University of Copenhagen and the capital region of Denmark. JH was supported by an industrial PhD grant from Innovation Fund Denmark. CHN was supported by the IBISS - Industrial Biomimetic Sensing and separation platform (http://www.ibiss.dtu.dk) funded by the Danish Innovation Fund Grant no. 097-2012-4.

6 Abbreviations/Nomenclature

A_0 - Initial polymersome surface area
A4F - Asymmetrical flow field-flow fractionation
AFM - Atomic force microscopy
Bd - 1,3-Butadiene
n-BuLi - *n*-Butyl lithium
n-Bu_2Mg - *n*-Dibutylmagnesium
CGMD - Coarse grain molecular dynamics
CLSM - Confocal laser scanning microscopy
d - Particle diameter
d_P - Polymersome diameter
DLS - Dynamic light scattering
DOPC - 1,2-dioleoyl-*sn*-glycero-3-phosphocholine
DPD - Dissipative particle dynamics
EM - Electron microscopy
EO - Ethylene oxide
EPR - Electron paramagnetic resonance
ESEM - Environmental scanning electron microscopy
ESRF - European Synchrotron Radiation Facility
f - Hydrophilic volume ratio
FACS - Fluorescence-activated cell-sorting
FCM - Flow cytometry
FCS - Fluorescence correlation microscopy
FF - Freeze fracture
FRM II - Forschungs-Neutronenquelle Heinz Maier-Leibnitz
FTLA - Finite track length adjustment
GPM - Generalized polarization microscopy
I - Light scattering intensity
ITO - Indium tin oxide
HPLC - High performance liquid chromatography
k - Rate constant of initial rise in stopped-flow light scattering curve
K_a - Elastic-area compressibility modulus
k_c - Bending elasticity modulus
Laurdan - 6-lauroyl-2-(dimethylamino)-naphthalene
LDE - Laser doppler electrophoresis
M_n - Number-averaged molecular weight
M_w - Weight-averaged molecular weight
MD - Molecular dynamics
NMR - Nuclear magnetic resonance
NNLS - Non-negatively constrained least squares
NS - Negative staining
NTA - Nanoparticle tracking analysis
OG - *n*-Octyl-β-D-Glucopyranoside
P_f - Bilayer permeablity
PAA - Polyacrylic acid
PB - 1,2-Polybutadiene
PCM - Phase contrast microscopy
PDI_M - Polydispersity index of the polymer length, defined as M_w/M_n
PDI_{DLS} - Polydispersity index of DLS analysis
PEO - Polyethylene oxide
PS - Polystyrene
q - X-ray and neutron scattering vector
R_P - Outer polymersome radius
RT - Room temperature
S - Vesicle surface area
SANS - Small-angle neutron scattering
SAXS - Small-angle x-ray scattering
SEC - Size exclusion chromatography
SDL - Size detection limit
SEM - scanning electron microscopy
SFLS - Stopped-flow light scattering
SLS - Static light scattering
STED - Stimulated emission depletion microscopy
STM - Scanning tunneling microscopy
t_P - Thickness of the hydrophobic core of polymersomes
tBuP4 - 1-*tert*-Butyl-4,4,4-tris(dimethylamino)-2,2-bis[tris (dimethyl-amino)-phosphoranylidenamino]-2λ^5,4λ^5-catenadi(phosphazene)
TEM - Transmission electron microscopy
THF - Tetrahydrofuran
TRPS - Tunable resistive pulse sensing
V_0 - Vesicle volume before osmotic shock at stopped-flow light scattering
V_w - Molar volume of water (10 cm^3/mol)
WAXS - Wide-angle x-ray scattering
Z_D - Intensity-weighted hydrodynamic diameter
α - Fractional surface area change of polymersomes
δ - Distribution width of polymersome diameter at DLS analysis
Δ_{osm} - Difference in osmolarity
ΔA - Polymersomes surface area change
θ - X-ray or neutron scattering angle
λ - Wavelength
τ - Isotropic tension change of the polymersome surface

References

1 L. Zhang and A. Eisenberg, *Science*, 1995, **268**, 1728–1731.
2 B. M. Discher, Y.-Y. Won, D. Ege, J. Lee, F. S. Bates, D. E. Discher and D. Hammer, *Science*, 1999, **284**, 1143–1146.
3 B. M. Discher, D. Hammer, F. S. Bates and D. E. Discher, *Curr. Opin. Colloid. In.*, 2000, **5**, 125–131.
4 C. Nardin, T. Hirt, J. Leukel and W. P. Meier, *Langmuir*, 2000, **16**, 1035–1041.
5 C. Nardin, J. Widmer, M. Winterhalter and W. P. Meier, *Eur. Phys. J. E*, 2001, **4**, 403–410.
6 D. E. Discher and A. Eisenberg, *Science*, 2002, **297**, 967–973.
7 M. Antonietti and S. Förster, *Adv. Mater.*, 2003, **15**, 1323–1333.
8 K. Kita-Tokarczyk, J. Grumelard, T. Haefele and W. P. Meier, *Polymer*, 2005, **46**, 3540–3563.
9 D. E. Discher and F. Ahmed, *Annu. Rev. Biomed. Eng.*, 2006, **8**, 323–341.
10 D. E. Discher, V. Ortiz, G. Srinivas, M. L. Klein, Y. Kim, D. Christian, S. Cai, P. Photos and F. Ahmed, *Prog. Polym. Sci.*, 2007, **32**, 838–857.
11 D. H. Levine, P. P. Ghoroghchian, J. Freudenberg, G. Zhang, M. J. Therien, M. I. Greene, D. A. Hammer and R. Murali, *Methods*, 2008, **46**, 25–32.

12 C. Lopresti, H. Lomas, M. Massignani, T. Smart and G. Battaglia, *J. Mater. Chem.*, 2009, **19**, 3557–3776.

13 M. Massignani, H. Lomas and G. Battaglia, *Advances in Polymer Sciences*, Springer, Berlin, Germany, 2010, pp. 115–154.

14 P. Tanner, P. Baumann, R. Enea, O. Onaca, C. G. Palivan and W. P. Meier, *Acc. Chem. Res.*, 2011, **44**, 1039–1049.

15 J. Liao, C. Wang, Y. Wang, F. Luo and Z. Qian, *Curr. Pharm. Design*, 2012, **18**, 3432–3441.

16 J. Nicolas, S. Mura, D. Brambilla, N. Mackiewicz and P. Couvreur, *Chem. Soc. Rev.*, 2013, **42**, 1147–1235.

17 J. Yang, H. Liu and X. Zhang, *Biotechnol. Adv.*, 2014, **32**, 804–817.

18 K. Langowska, C. G. Palivan and W. P. Meier, *Chem. Commun.*, 2013, **49**, 128–130.

19 P. V. Pawar, S. V. Gohil, J. P. Jain and N. Kumar, *Polym. Chem.*, 2013, **4**, 3160–3176.

20 R. Langer, *Science*, 1990, **249**, 1527–1533.

21 S. Egli, M. Nussbaumer, V. Balasubramanian, M. Chami, N. Bruns, C. G. Palivan and W. P. Meier, *J. Am. Chem. Soc*, 2011, **133**, 4476–4483.

22 L. Kuang, D. A. Fernandes, M. O'Halloran, W. Zheng, Y. Jiang, V. Ladizhansky, L. S. Brown and H. Liang, *ACS Nano*, 2014, **8**, 537–545.

23 H.-J. Choi and C. D. Montemagno, *Nano Lett.*, 2005, **5**, 2538–2542.

24 V. Malinova, M. Nallani, W. P. Meier and E. K. Sinner, *FEBS Lett.*, 2012, **586**, 2146–2156.

25 A. González-Pérez, K. Stibius, T. Vissing, C. Hélix-Nielsen and O. G. Mouritsen, *Langmuir*, 2009, **25**, 10447–10450.

26 M. Sauer, T. Haefele, A. Graff, C. Nardin and W. P. Meier, *Chem. Commun.*, 2001, **23**, 2452–2453.

27 C. Hélix-Nielsen, *Anal. Bioanal. Chem.*, 2009, **395**, 697–718.

28 Nanyang Technological University, Aquaporin AS, C. Y. Tang, C. Qiu, Y. Zhao, W. Shen, A. Vararattanavech, R. Wang, X. Hu, J. Torres, A. G. Fane and C. Hélix-Nielsen, Aquaporin based thin film composite membranes, WO 2013/043118, 2013.

29 C. Y. Tang, Y. Zhao, R. Wang, C. Hélix-Nielsen and A. G. Fane, *Desalination*, 2013, **308**, 34–40.

30 P. S. Zhong, T.-S. Chung, K. Jeyaseelan and A. Armugam, *J. Membr. Sci.*, 2012, **407-408**, 27–33.

31 H. L. Wang, T.-S. Chung, Y. W. Tong, K. Jeyaseelan, A. Armugam, H. H. P. Duong, F. Fu, H. Seah, J. Yang and M. Hong, *J. Membr. Sci.*, 2013, **434**, 130–136.

32 B. J. Berne and R. Pecora, *Dynamic light scattering*, Courier Dover Publications, Mineola, NY, USA, 2000.

33 O. Glatter and O. Kratky, *Small Angle X-ray Scattering*, Academic Press, London, UK, 1982.

34 I. Grillo, *Small-Angle Neutron Scattering andApplications in SoftCondensed Matter*, Springer, Heidelberg, Germany, 2008.

35 J. S. Pedersen, *Adv. Colloid Interface Sci.*, 1997, **70**, 171–210.

36 B. Carr, M. Wright and Nanosight, 2013, 1–193.

37 R. A. Dragovic, C. Gardiner, A. S. Brooks, D. S. Tanetta, D. J. Ferguson, P. Hole, B. Carr, C. W. G. Redman, A. L. Harris, P. J. Dobson, P. Harrison and I. L. Sargent, *Nanomed. Nanotech. Biol. Med.*, 2011, **7**, 780–788.

38 C. Gardiner, Y. J. Ferreira, R. A. Dragovic, C. W. G. Redman and I. L. Sargent, *J. Extracell. Vesicles*, 2013, **2**, 19671.

39 K. Edwards and A. Baeumner, *Talanta*, 2006, **68**, 1432–1441.

40 B. Ruozi, G. Tosi, E. Leo and M. Vandelli, *Talanta*, 2007, **73**, 12–22.

41 E. Tomaszewska, K. Soliwoda, K. Kadziola, B. Tkacz-Szczesna, G. Celichowski, M. Cichomski, W. Szmaja and J. Grobelny, *J. Nanomater.*, 2013, **2013**, 313081.

42 S. Hupfeld, A. M. Holsæter, M. Skar, C. B. Frantzen and M. Brandl, *J. Nanosci. Nanotechnol.*, 2006, **6**, 3025–3031.

43 X. Zhang, P. Tanner, A. Graff, C. G. Palivan and W. P. Meier, *J. Polym. Sci. A Polym. Chem.*, 2012, **50**, 2293–2318.

44 Y. Won, A. K. Brannan, H. Davis and F. S. Bates, *J. Phys. Chem. B*, 2002, **106**, 3354–3364.

45 S.-H. Choi, F. S. Bates and T. P. Lodge, *Macromolecules*, 2014, **47**, 7978–7986.

46 J. Braun, N. Bruns, T. Pfohl and W. P. Meier, *Macromol. Chem. Phys.*, 2011, **212**, 1245–1254.

47 M. Hirai, R. Kimura, K. Takeuchi, Y. Hagiwara, R. Kawai-Hirai, N. Ohta, N. Igarashi and N. Shimuzu, *J. Synchrotron Rad.*, 2013, **20**, 869–874.

48 A. I. Norman, J. T. Cabral, A. Karim and E. J. Amis, *Macromol. Rapid Commun.*, 2004, **25**, 307–311.

49 U. Till, M. Gaucher-Delmas, P. Saint-Aguet, G. Hamon, J.-D. Marty, C. Chassenieux, B. Payré, D. Goudounèche, A.-F. Mingotaud and F. Violleau, *Anal. Bioanal. Chem.*, 2014, **406**, 7841–7853.

50 Y. Won, H. Davis and F. S. Bates, *Macromolecules*, 2003, **36**, 953–955.

51 P. S. Ho, J. Leu and W. W. Lee, *Low Dielectric Constant Materials for IC Applications*, Springer, Berlin, Germany, 2003.

52 M. Kumar, J. Habel, Y.-x. Shen, W. P. Meier and T. Walz, *J. Am. Chem. Soc*, 2012, **134**, 18631–18637.

53 E. van der Pol, F. A. W. Coumans, A. E. Grootemaat, C. Gardiner, I. L. Sargent, P. Harrison, A. Sturk, T. G. van Leeuwen and R. Nieuwland, *J. Thromb. Haemost.*, 2014, **12**, 1182–1192.

54 C. Chen, S. Zhu, T. Huang, S. Wang and X. Yan, *Anal. Methods*, 2013, **5**, 2150–2157.

55 J. P. Jain, W. Y. Ayen and N. Kumar, *Curr. Pharm. Design*, 2011, **17**, 65–79.

56 A. A. Reinecke and H.-G. Döbereiner, *Langmuir*, 2003, **19**, 605–608.

57 http://www.microbehunter.com/phase-contrast-vs-bright-field microscopy/.

58 J. S. Hansen and C. Hélix-Nielsen, *Biochem. Biophys. Res. Commun.*, 2011, **415**, 686–690.

59 M. Erbakan, Y.-x. Shen, M. Grzelakowski, P. J. Butler, M. Kumar and W. R. Curtis, *PLoS ONE*, 2014, **9**, e86830.

60 B. Ruozi, D. Belletti, A. Tombesi, G. Tosi, L. Bondioli, F. Forni and M. A. Vandelli, *Int. J. Nanomedicine*, 2011, **6**, 557–563.

61 A. H. Kunding, M. W. Mortensen, S. M. Christensen and D. Stamou, *Biophys. J.*, 2008, **95**, 1176–1188.

62 S. W. Hell, *Science*, 2007, **316**, 1153–1158.

63 J. Habel, A. Ogbonna, N. Larsen, L. Schulte, K. Almdal and C. Hèlix-Nielsen, *J. Polym. Sci. B Polym. Phys.*, submitted.

64 B. Coldren, R. van Zanten, M. J. Mackel, J. A. Zasadzinski and H.-T. Jung, *Langmuir*, 2003, **19**, 5632–5639.

65 Y.-Y. Won, *Korean J. Chem. Eng.*, 2004, **21**, 296–302.

66 J. K. Harris, G. D. Rose and M. L. Bruening, *Langmuir*, 2002, **18**, 5337–5342.

67 D. C. Joy, *J. Microsc.*, 1984, **136**, 241–258.

68 F. J. Doucet, J. R. Lead, L. Maguire, E. P. Achterberg and G. E. Millward, *J. Environ. Monitor.*, 2005, **7**, 115–121.

69 S. Li and A. F. Palmer, *Macromolecules*, 2005, **38**, 5686–5698.

70 M. R. Mozafari, M. H. Zareie, E. Piskin and V. Hasirci, *Drug Deliv.*, 1998, **5**, 135–141.

71 C. Bai, *Scanning Tunneling Microscopy and Its Application*, Springer, Heidelberg, Germany, 2nd edn, 2000, vol. 32.

72 B. Baruah and A. Surin, *J. Biol. Inorg. Chem.*, 2012, **17**, 899–910.

73 Y. P. Patil and S. Jadhav, *Chem. Phys. Lipids*, 2014, **177**, 8–18.

74 A. Laouini, C. Jaafar-Maalej, I. Limayem-Blouza, S. Sfar, C. Charcosset and H. Fessi, *J. Colloid Sci. Biotechnol.*, 2012, **1**, 147–168.

75 K. Takeshita and T. Ozawa, *J. Radiat. Res.*, 2004, **45**, 373–384.

76 D. Wu, M. Spulber, F. Itel, M. Chami, T. Pfohl, C. G. Palivan and W. P. Meier, *Macromolecules*, 2014, **47**, 5060–5069.

77 C. Matos, B. de Castro, P. Gameiro, J. L. F. C. Lima and S. Reis, *Langmuir*, 2004, **20**, 369–377.

78 J. A. Schwarz and C. I. Contescu, *Surfaces of Nanoparticles and Porous Materials*, CRC Press, New York, NY, USA, 1st edn, 1999, vol. 78.

79 R. Dimova, U. Seifert, B. Pouligny, S. Förster and H.-G. Döbereiner, *Eur. Phys. J. E*, 2002, **7**, 241–250.

80 S. Dieluweit, A. Csiszár, W. Rubner, J. Fleischhauer, S. Houben and R. Merkel, *Langmuir*, 2010, **26**, 11041–11049.

81 R. R. Jahan-Tigh, C. Ryan, G. Obermoser and K. Schwarzenberger, *j. Invest. Dermatol.*, 2012, **132**, e1.

82 D. Burger, S. Schock, C. S. Thompson, A. C. Montezano, A. M. Hakim and R. M. Touyz, *Clin. Sci.*, 2013, **124**, 423–441.

83 M. Holzer, S. Barnert, J. Momm and R. Schubert, *J. Chromatogr. A*, 2009, **1216**, 5838–5848.

84 C. Grabielle-Madelmont, S. Lesieur and M. Ollivon, *J. Biochem. Biophys. Methods*, 2003, **56**, 189–217.

85 Z. Zhong, Q. Ji and J. A. Zhang, *J. Pharm. Biomed. Anal.*, 2010, **51**, 947–951.

86 L. Yang, M. F. Broom and I. G. Tucker, *Pharm. Res.*, 2012, **29**, 2578–2586.

87 J. N. Sachs, P. S. Crozier and T. B. Woolf, *J. Chem. Phys.*, 2004, **121**, 10847.

88 G. Srinivas, D. E. Discher and M. Klein, *Nano Lett.*, 2005, **5**, 2343–2349.

89 M. Xiao, J. Liu, J. Yang, R. Wang and D. Xie, *Soft Matter*, 2013, **9**, 2434–2442.

90 L. Reimer, *Transmission Electron Microscopy : Physics of Image Formation*, Springer, New York, NY, USA, 5th edn, 2008.

91 D. McMullan, *Scanning*, 1995, **17**, 175–185.

92 G. D. Danilatos, *Advances in Electronics and Electron Physics*, Academic Press, San Diego, CA, USA, 1988, pp. 109–250.

93 A. Cavalier, D. Spehner and B. M. Humbel, *Handbook of cryopreparation methods for electron microscopy*, CRC Press, Boca Raton, FL, USA, 2008.

94 J. Pawley, *Handbook of Biological Confocal Microscopy*, Springer, Berlin, Germany, 3rd edn, 2006.

95 L. A. Bagatolli, *Biochim. Biophys. Acta - Biomembr.*, 2006, **1758**, 1541–1556.

96 F. J. Giessibl, *Rev. Mod. Phys.*, 2003, **75**, 949–983.

97 C. Rein, K. Pszon-Bartosz, K. B. Stibius, T. Bjørnholm and C. Hélix-Nielsen, *Langmuir*, 2011, **27**, 499–503.

98 Y. Chen, *PhD thesis*, Washington University, St. Louis, MO, USA, 2008.

99 R. M. Hochmuth, *J. Biomech.*, 2000, **33**, 15–22.

100 R. Dimova, C. Dietrich, A. Hadjiisky, K. Danov and B. Pouligny, *Eur. Phys. J. B*, 1999, **12**, 589–598.

101 V. Chechik and D. M. Murphy, *Electron Paramagnetic Resonance*, RSC, London, UK, 2014, vol. 24.

102 J. Keeler, *Understanding NMR Spectroscopy*, Jon Wiley & Sons, Hoboken, NJ, USA, 2nd edn, 2010.

103 M. G. Omerod, *Flow Cytometry - A practical approach*, Oxford University Press, Oxford, UK, 3rd edn, 2000.

104 A. M. Striegel, J. J. Kirkland, W. W. Yau and D. D. Bly, *Modern Size Exclusion Chromatography: Practice of Gel Permeation and Gel Filtration Chromatography*, Jon Wiley & Sons, Hoboken, NJ, USA, 2nd edn, 2009.

105 C. Bria, F. Violleau and S. K. R. Williams, *LC GC Europe*, 2013, **26**, 660–671.

106 S. Förster and E. Krämer, *Macromolecules*, 1999, **32**, 2783–2785.

107 S. Jain, M. H. E. Dyrdahl, X. Gong, L. E. Scriven and F. S. Bates, *Macromolecules*, 2008, **41**, 3305–3316.

108 J. A. Zupancich, F. S. Bates and M. A. Hillmyer, *Biomacromolecules*, 2009, **10**, 1554–1563.

109 J. Lee, H. Bermudez, B. M. Discher, M. Sheehan, Y.-Y. Won, F. S. Bates and D. E. Discher, *Biotechnol. Bioeng.*, 2001, **73**, 135–145.

110 J. R. Howse, R. A. L. Jones, G. Battaglia, R. E. Ducker, G. J. Leggett and A. J. Ryan, *Nat. Mater.*, 2009, **8**, 507–511.

111 S. U. Egelhaaf, E. Wehrli, M. Muller, M. Adrian and P. Schurtenberger, *J. Microsc.*, 1996, **184**, 214–228.

112 G. Battaglia, C. Lopresti, M. Massignani, N. J. Warren, J. Madsen, S. Forster, C. Vasilev, J. K. Hobbs, S. P. Armes, S. Chirasatitsin and A. J. Engler, *Small*, 2011, **7**, 2010–2015.

113 O. Stauch, T. Uhlmann, M. Fröhlich, R. Thomann, M. El-Badry, Y.-K. Kim and R. Schubert, *Biomacromolecules*, 2002, **3**, 324–332.
114 M. Kumar, M. Grzelakowski, J. Zilles, M. M. Clark and W. P. Meier, *Proc. Natl. Acad. Sci. USA*, 2007, **104**, 20719–20724.
115 M. I. Angelova and D. S. Dimitrov, *Faraday Discuss. Chem. Soc.*, 1986, **81**, 303–311.
116 E. Evans, W. Rawicz and B. A. Smith, *Faraday Discuss.*, 2013, **161**, 591–611.
117 W. Rawicz, K. C. Olbrich, T. McIntosh, D. Needham and E. Evans, *Biophys. J.*, 2000, **79**, 328–339.
118 G. Mie, *Ann. Phys.*, 1908, **330**, 377–445.
119 P. A. Hassan and S. K. Kulshreshtha, *J. Colloid Interface Sci.*, 2006, **300**, 744–748.
120 C. F. Bohren, *The Scattering of light & other electromagnetic radiation*, Jon Wiley & Sons, New York, NY, USA, 1983.
121 L. Ma and A. Eisenberg, *Langmuir*, 2009, **25**, 13730–13736.
122 K. P. Ryan, *Scanning Microsc.*, 1992, **6**, 715–743.
123 L. P. Aggerbeck and T. Gulik-Krzywicki, *Methods Enzymol.*, 1986, **128**, 457–472.
124 H. Bermudez, A. K. Brannan, D. A. Hammer, F. S. Bates and D. E. Discher, *Macromolecules*, 2002, **35**, 8203–8208.
125 F. Itel, M. Chami, A. Najer, S. Lörcher, D. Wu, I. A. Dinu and W. P. Meier, *Macromolecules*, 2014, **47**, 7588–7596.
126 R. Hite, S. Raunser and T. Walz, *Curr. Opin. Struc. Biol.*, 2007, **17**, 389–395.
127 L. Fetters, W. Graessley, R. Krishnamoorti and D. Lohse, *Macromolecules*, 1997, **30**, 4973–4977.
128 P. Walde and S. Ichikawa, *Biomol. Eng.*, 2001, **18**, 143–177.
129 E. Evans and D. Needham, *J. Phys. Chem.*, 1987, **91**, 4219–4228.
130 A. Carlsen, N. Glaser, J.-F. Le Meins and S. Lecommandoux, *Langmuir*, 2011, **27**, 4884–4890.
131 J.-L. Rigaud and D. Levy, *Methods Enzymol.*, 2003, **372**, 65–86.
132 J. C. Mathai, S. Tristram-Nagle, J. F. Nagle and M. L. Zeidel, *J. Gen. Physiol.*, 2008, **131**, 69–76.
133 F. M. Menger and M. I. Angelova, *Acc. Chem. Res.*, 1998, **31**, 789–797.
134 S. A. Sanchez, M. A. Tricerri, G. Gunter and E. Gratton, *Modern Research and Educational Topics in Microscopy*, Formatex, Extremadura, Spain, 2007, pp. 1007–1014.
135 H. Aranda-Espinoza, H. Bermudez, F. S. Bates and D. E. Discher, *Phys. Rev. Lett.*, 2001, **87**, 208301.
136 J. Habel, A. Ogbonna, N. Larsen, S. Krabbe, K. Almdal and C. Hèlix-Nielsen, *Physical Chemistry Chemical Physics*, submitted.
137 R. W. O'Brien, B. R. Midmore, A. Lamb and R. J. Hunter, *Faraday Discuss. Chem. Soc.*, 1990, **90**, 301–312.
138 B. D. Coday, T. Luxbacher, A. E. Childress, N. Almaraz, P. Xu and T. Y. Cath, *J. Membr. Sci.*, 2015, **478**, 58–64.
139 F. Itel, S. Al-Samir, F. Oberg, M. Chami, M. Kumar, C. T. Supuran, P. M. T. Deen, W. P. Meier, K. Hedfalk, G. Gros and V. Endeward, *FASEB J.*, 2012, **26**, 5182–5191.